

1 Towards Improved Prediction of the Bedrock Depth
2 Underneath Hillslopes: Bayesian Inference of the
3 Bottom-up Control Hypothesis using
4 High-Resolution Topographic Data

Guilherme J. C. Gomes,^{1,2} Jasper A. Vrugt,^{2,3,*} and Eurípedes A. Vargas Jr.¹

* Corresponding author: Jasper A. Vrugt, Department of Civil and Environmental Engineering,
University of California, Irvine, California, USA. (jasper@uci.edu)

¹Departamento de Engenharia Civil,
Pontifícia Universidade Católica do Rio de
Janeiro, Rio de Janeiro, Brazil.

²Department of Civil and Environmental
Engineering, University of California,
Irvine, California, USA.

³Department of Earth System Science,
University of California, Irvine, California,
USA.

Key Points.

- We introduce an analytic formulation for the spatial distribution of the bedrock depth
- Bayesian analysis reconciles our model with field data and quantifies prediction and parameter uncertainty
- The use of a distributed parametrization recognizes geologic heterogeneities

5 **Abstract.** The depth to unweathered bedrock controls a myriad of at-
6 mospheric, ecologic, geomorphologic, and hydrologic processes by influencing
7 subsurface flow paths, erosion rates, soil moisture status, water uptake by
8 plant roots, and latent and sensible heat fluxes. As hillslope interiors are very
9 difficult and costly to illuminate and access, the topography of the bedrock
10 surface is largely unknown. This essay is concerned with the prediction of
11 spatial patterns in the depth to bedrock (DTB) using high-resolution topo-
12 graphic data, numerical modeling and Bayesian analysis. Our DTB model
13 builds on the bottom-up control on fresh-bedrock topography hypothesis of
14 *Rempe and Dietrich* [2014] and includes a mass movement and bedrock-valley
15 morphology term to extend the usefulness and general applicability of the
16 model to convex, concave, planar, convergent and divergent hillslopes. Most
17 of the parameters of the DTB model represent physical entities that can be
18 measured directly in the laboratory or field, and simulated variables can be
19 verified with geophysical imaging, drilling, cosmogenic nuclide measurements,
20 and topographic surveying. We reconcile the DTB model with field obser-
21 vations using Bayesian analysis with the DREAM algorithm [*Vrugt et al.*,

22 2008, 2009]. We investigate explicitly the benefits of using spatially distributed
23 parameter values to account implicitly, and in a relatively simple way, for
24 rock mass heterogeneities that are very difficult, if not impossible, to char-
25 acterize adequately in the field. We illustrate our method using an artificial
26 data set of bedrock depth observations and then evaluate our DTB model
27 with real-world data collected at the Papagaio river basin in Rio de Janeiro,
28 Brazil. Our results demonstrate that the DTB model predicts accurately the
29 observed bedrock depth data. The posterior mean DTB simulation is shown
30 to be in good agreement with the measured bedrock depth data. The pos-
31 terior prediction uncertainty of the DTB model can be propagated forward
32 through hydromechanical models to derive probabilistic estimates of land-
33 slide potential and factors of safety.

1. INTRODUCTION

34 The depth to bedrock (DTB) controls a large array of geomorphologic, hydrologic,
35 geochemical, ecologic and atmospheric processes, yet is large unknown as hillslope interiors
36 are very difficult and costly to illuminate and access. The regolith thickness determines
37 groundwater flow [*Freer et al.*, 2002; *Lanni et al.*, 2012], infiltration and redistribution
38 [*Kosugi et al.*, 2006], subsurface saturation [*Tromp-van Meerveld and McDonnell*, 2006b;
39 *Ebel et al.*, 2007; *Liang and Uchida*, 2014], runoff generation [*Troch et al.*, 2002; *Tromp-*
40 *van Meerveld and McDonnell*, 2006a], storage capacity [*Ohnuki et al.*, 2008], the shape of
41 the hydrograph [*Hopp and McDonnell*, 2009], and variably saturated water flow [*Fujimoto*
42 *et al.*, 2008]. The bedrock topography is also of paramount importance in geotechnical
43 engineering as it determines slope stability [*Mukhlisin et al.*, 2008; *Ho et al.*, 2012; *Kim*
44 *et al.*, 2015], pore pressure responses to infiltration [*Vargas Jr. et al.*, 1990; *Askarinejad*
45 *et al.*, 2012; *Lanni et al.*, 2013], and landslide potential [*Borja and White*, 2010; *Milledge*
46 *et al.*, 2014; *Bellugi et al.*, 2015]. An accurate characterization of the DTB is thus a
47 prerequisite to describe accurately many different Earth-surface processes.

48 Spatial patterns in the bedrock depth arise from complex interactions between a myr-
49 iad of biologic [*Jenny*, 1941], (geo)chemical [*Lebedeva and Brantley*, 2013], and hydrologic
50 [*Rempe and Dietrich*, 2014] processes, and factors including surface topography, lithology
51 [*Catani et al.*, 2010], climate [*Anderson et al.*, 2013], and long-term human activities [*Kuri-*
52 *akose et al.*, 2009]. As a consequence, the thickness of the regolith can vary considerably
53 within a hillslope and watershed, thereby complicating tremendously the characterization
54 and point prediction of the bedrock depth topography [*Catani et al.*, 2010]. Until hillslope

55 interiors are more readily accessible through geophysical imaging or extensive deep drilling
56 the transition of the underlying fresh bedrock will remain largely unknown [*Rempe and*
57 *Dietrich, 2014*].

58 During the past decades a great deal of research has been devoted to characterization
59 of the soil and regolith depth in headwater hillslopes and catchments. That research has
60 focused primarily on four different issues: (1) the development of specialized measure-
61 ment techniques for (in)direct observation of the bedrock depth, (2) the application and
62 use of interpolation methods to predict the bedrock depths from sparse direct observa-
63 tions and/or secondary data, (3) the development and application of empirico-statistical
64 methods that predict the spatial continuum of the regolith depth with the help of eas-
65 ily measurable environmental covariates, and (4) the development of landscape evolution
66 models that predict the soil/regolith depth by solving numerically or analytically the soil
67 mass conservation equation.

68 Research into measurement methods has led to the development and use of direct and
69 indirect sensing techniques to determine the bedrock depth at point and larger support.
70 Examples of direct measurement methods include rod penetrometers [*Kuriakose et al.,*
71 *2009; Tesfa et al., 2009; Fu et al., 2011; Lanni et al., 2012; Lucà et al., 2014*], excavated
72 pits [*Boer et al., 1996; Heimsath et al., 2001; Pelletier and Rasmussen, 2009; Catani et*
73 *al., 2010; Pelletier et al., 2011*], hand and gasoline or electric-powered augers [*Fernandes*
74 *et al., 1994; Ziadat, 2010; Liu et al., 2013*], road cuts and erosion gullies [*Kuriakose et*
75 *al., 2009; Wilford and Thomas, 2013*], and dynamic cone penetrometers [*Kosugi et al.,*
76 *2006, 2009; Fujimoto et al., 2008; Ohnuki et al., 2008; Tsuchida et al., 2011; Askarinejad et*
77 *al., 2012; Wiegand et al., 2013; Athapaththu et al., 2014; Liang and Uchida, 2014*]. This last

78 measurement device is particularly promising as it can help delineate soil stratigraphy and
79 layers with contrasting hydraulic properties [Eguchi et al., 2009; Masaoka et al., 2012].
80 Examples of indirect bedrock depth measurement methods include the use of gravity
81 survey [Stewart, 1980; Bohidar et al., 2001], geophysical exploration [Dahlke et al., 2009],
82 seismic refraction [Zhou and Wu, 1994], electrical resistivity tomography [Zhou et al.,
83 2000; Lucà et al., 2014], and airborne electromagnetic [Christensen et al., 2015]. These
84 latter five measurement methods make it possible to determine noninvasively the physical
85 properties of the subsurface, yet inversion methods are required to interpret these indirect
86 observations of the bedrock depth. Much effort is required to use these measurement
87 methods to characterize bedrock depth variations at the spatial scale of a hillslope or
88 watershed.

89 Research into interpolation methods has led to the development and use of (non)linear
90 regression methods to derive regolith depth maps compatible with the application scale
91 of hydrologic and/or geotechnical models. These methods can be classified in two main
92 groups including deterministic and geostatistical interpolation approaches. Deterministic
93 interpolation techniques create a bedrock depth map from measured DTB observations,
94 based on either the extent of similarity between nearby regolith depth observations or the
95 degree of smoothing. Examples include the use of triangulated irregular networks [Kim
96 et al., 2015], inverse distance weighting [Stewart, 1980] and radial basis functions, and
97 these approaches work well in the absence of spatial correlation between the measured
98 regolith depth data [Freer et al., 2002; Wiegand et al., 2013]. Geostatistical interpolation
99 techniques capitalize on the spatial structure and semi-variance of the measured bedrock
100 depth data [Goovaerts, 1997]. Examples include ordinary kriging [Sitharam et al., 2008;

101 *Tye et al.*, 2011], cokriging [*Chung and Rogers*, 2012], and regression-kriging [*Odeh et*
102 *al.*, 1995; *Sarkar et al.*, 2013]. These methods can incorporate topographic control points
103 derived from digital elevation models and other primary (topographic variables) and sec-
104 ondary (other covariates) variables. Conditional stochastic (Gaussian) simulation can be
105 used to better represent the short-range regolith depth variability derived from geostatistical
106 interpolation [*Kuriakose et al.*, 2009; *Lucà et al.*, 2014]. Interpolation methods are
107 easy to use in practice but require large amounts of field data to derive high-resolution
108 and high-fidelity maps of the bedrock surface topography [*Dietrich et al.*, 1995; *Catani et*
109 *al.*, 2010; *Liu et al.*, 2013].

110 Research into empirico-statistical methods has led to the development of multivariate
111 linear/nonlinear or logistic regression methods that predict the bedrock depth from envi-
112 ronmental covariates deemed important in soil and regolith formation. These soil-forming
113 factors have been discussed by *Jenny* [1941] in his infamous equation and include cli-
114 mate, organisms, relief, parent material, and time. Topographic variables (terrain and
115 landform), bedrock properties (geology and geochemistry) and climatologic characteris-
116 tics (radiation, precipitation and temperature) have all been used as predictors of the
117 regolith depth in regression models [*DeRose et al.*, 1991; *Boer et al.*, 1996; *Ziadat*, 2010;
118 *Wilford and Thomas*, 2013; *Yang et al.*, 2014]. Other regression-type methods published
119 in the geomorphologic literature include the use of artificial neural networks [*Zhou and*
120 *Wu*, 1994; *Mey et al.*, 2015], principal component analysis and maximum likelihood clas-
121 sification [*Boer et al.*, 1996; *Ziadat*, 2005], canonical correspondence analyses [*Odeh et al.*,
122 1991], support vector machines [*Sitharam et al.*, 2008], and generalized additive models
123 and random forests [*Tesfa et al.*, 2009; *Shafique et al.*, 2011]. These latter two methods

124 use secondary data of land cover and other soil attributes derived from remote sensing
125 products. Although regression methods have the advantage of being practical and rela-
126 tively easy to use, the relationship between the regolith depth and exogenous variables
127 (covariates) is empirical and poorly rooted in geomorphologic theory. This complicates
128 their application to out-of-sample prediction in areas outside the domain spanned by the
129 observations.

130 Research into modeling approaches has led to the development of landscape evolution
131 models that solve the soil mass-balance equation over geological time scales using forward
132 [*Dietrich et al.*, 1995; *Roering*, 2008] or backward simulation [*Pelletier et al.*, 2011]. These
133 geomorphic models simulate processes such as tectonic uplift, regolith production by the
134 underlying bedrock, colluvial transport of the unconsolidated material, erosion and sed-
135 imentation, and have shown to be particularly useful for validation of field observations
136 and hypothesis testing of different soil transport equations. However, the output of land-
137 scape evolution models is subject to considerable uncertainty due to errors in the initial
138 states (e.g. topography one or more relief replacement times ago), boundary conditions
139 (climate and tectonic forcing), geologic characterization (e.g. bedrock properties), param-
140 eter values, model structure and equations. If conditions of dynamic equilibrium between
141 soil production and erosion are assumed, then simple closed-form parametric solutions
142 can be derived for the soil thickness by solving analytically the soil conservation equa-
143 tion for certain specific formulations of the soil transport equation and/or soil production
144 function [*Bertoldi et al.*, 2006; *Saco et al.*, 2006; *Pelletier and Rasmussen*, 2009]. These
145 analytic solutions allow for predictive mapping of the soil thickness from high-resolution
146 topographic data and field-based calibration [*Pelletier and Rasmussen*, 2009]. Examples

147 include the nonlinear slope-dependent, nonlinear depth- and slope-dependent, and non-
148 linear area- and slope-dependent transport functions of *Pelletier and Rasmussen* [2009].
149 These analytic models describe accurately thin soil depth beneath hillslope ridges, but
150 it has yet to be established whether they can predict accurately concave hillslopes with
151 relatively thin soils. This may give preference instead to simulation of instantaneous DTB
152 maps using high-resolution topographic data [*Saulnier et al.*, 1997; *Bertoldi et al.*, 2006;
153 *Catani et al.*, 2010].

154 In a separate line of research, *Catani et al.* [2010] have proposed an empirical
155 geomorphology-based model to predict the bedrock depth at the catchment scale using
156 relative position, hillslope gradient and curvature. This model was shown to describe ac-
157 curately the observed regolith depths of Italian watersheds. *Liu et al.* [2013] have derived
158 a simple analytic expression of the soil mass balance equation for humid and semi-humid
159 climates without tectonic activity in the immediate geological past. The simulated soil
160 depths of this model match closely the observed bedrock depths at the 7.9 ha Shale Hills
161 catchment in the USA with root mean square error of 0.39 m and $R^2 = 0.74$. These
162 closed-form analytic models of the regolith thickness are much easier to implement and
163 use in practice than numerical landscape evolution models requiring only a high-resolution
164 topographic map and some calibration against observed regolith depth data to predict the
165 bedrock surface. Recently, *Rempe and Dietrich* [2014] have introduced an alternative an-
166 alytic model that predicts the hillslope form and the vertical extent of the weathered rock
167 underling soil-mantled hillslopes using physical parameters such as permeability of the
168 intact rock mass, porosity, and the rate of channel incision at the base of the hillslope.
169 This model builds on the assumption that once the fresh bedrock, saturated with nearly

170 stagnant fluid, is advected into the near surface through uplift and erosion, channel inci-
171 sion produces a lateral head gradient within the fresh bedrock inducing drainage toward
172 the channel. The slow drainage of the fresh bedrock exerts an bottom-up control on the
173 advance of the weathering front, suggesting that bedrock discontinuities and fractures can
174 play a major role in regolith production [*Clair et al.*, 2015]. The model of *Rempe and*
175 *Dietrich* [2014] produces thick weathered zones beneath ridges and thin regolith depths
176 beneath valleys, and has the advantage of being fully testable. Most of the model param-
177 eters can be measured directly in the laboratory or field using experiments on soil and
178 rock mass samples, and the simulated variables can be verified using cosmogenic nuclide
179 measurements, geophysical imaging, topographic surveying, and drilling.

180 Whereas much progress has been made on the development and use of models for pre-
181 diction of the regolith thickness, surprisingly little attention has been given to inference
182 of their parameters. Many of the parameters in these models cannot be measured directly
183 in the field but can only be meaningfully inferred from field data. What is more, some
184 parameters might be depth-dependent or vary spatially depending on hillslope position
185 and lithology. In this paper, we build on the ideas of *Pelletier and Rasmussen* [2009],
186 *Catani et al.* [2010] and *Rempe and Dietrich* [2014] and introduce a Bayesian framework
187 for DTB model parameter estimation. The Bayesian paradigm provides a simple way to
188 address systematically different sources of uncertainty within a single cohesive, integrated
189 framework [*Vrugt et al.*, 2008]. We use Markov chain Monte Carlo (MCMC) simulation
190 with the DiffeRential Evolution Adaptive Metropolis (DREAM) algorithm [*Vrugt et al.*,
191 2008, 2009] to infer the parameters of the DTB model from spatially distributed regolith
192 depth observations. This model builds on the bottom up control of fresh bedrock hy-

193 pothesis of *Rempe and Dietrich* [2014] and uses a slope-dependency and a bedrock-valley
194 shape term to extent the usefulness and general applicability of the model. The DREAM
195 algorithm has been applied to many different fields of study involving lumped [*He et*
196 *al.*, 2011; *Scharnagl et al.*, 2011] and spatially distributed, high-dimensional, parameter
197 spaces [*Keating et al.*, 2010; *Laloy et al.*, 2013; *Linde and Vrugt*, 2013; *Lochbühler et al.*,
198 2014]. We investigate explicitly the benefits of using spatially distributed DTB parame-
199 ter values for the prediction of bedrock depths. Such parameterization provides a means
200 to account implicitly, and in a relatively simple way, for system heterogeneities that are
201 difficult, or impossible, to characterize adequately in the field. We illustrate our method
202 using synthetic bedrock depth observations and validate our approach with real-world
203 data collected at the Papagaio river basin (PRB) in Rio de Janeiro, Brazil. The PRB
204 watershed has been the subject of much study in the literature [*Guimarães et al.*, 2003;
205 *Fernandes et al.*, 2004; *Vieira and Fernandes*, 2004; *Gomes et al.*, 2008, 2013] but this
206 previous work has focused primarily on unraveling the mechanisms of mass movement
207 rather than modeling of the bedrock depth.

208 The remainder of this paper is organized as follows. Section 2 reviews the basic building
209 blocks of the DTB model. Then in section 3, we evaluate the sensitivity of each of the DTB
210 model parameters to the simulated bedrock surface for a synthetic hillslope topography.
211 This section will help build awareness and intuition on how the different DTB model
212 parameters affect the simulated bedrock profiles. This is followed in section 4 with a short
213 introduction to Bayesian analysis (inversion) for inference of the DTB model parameters.
214 In this section we are especially concerned with the description of the DREAM algorithm
215 used to sample the posterior parameter distribution. We then proceed with a discussion

216 of the DTB inversion results for a synthetic (section 5) and real-world (section 6) regolith
217 depth data set using lumped and spatially distributed parameter values. Section 7 of this
218 paper discusses the implications of our results for hydrologic and geotechnical modeling
219 and engineering. Finally, section 8 concludes this paper with a summary of the main
220 findings.

2. MODEL DESCRIPTION

221 In this section, we introduce the different building blocks of our DTB model which
222 is used herein to predict the hillslope form and the vertical extent of the weathered
223 rock underling soil-mantled hillslopes from a high-resolution topographic map of the soil
224 surface. We assume herein that regolith thickness depends on the interplay between
225 erosion, which removes unconsolidated material from the ground surface, and weathering,
226 which promotes rock fragmentation in the soil-bedrock interface. Our model builds on
227 the bottom-up control on fresh-bedrock hypothesis of *Rempe and Dietrich* [2014] and
228 calculates the thickness of the weathered zone from the difference between the measured
229 surface topography and predicted groundwater profile derived from analytic solution of
230 the one-dimensional steady-state Boussinesq equation [*Bear*, 2013]. Two additional terms
231 are used to characterize adequately the morphology of the bedrock surface beneath the
232 drainage valley, and the regolith thickness on steep slopes subject to an increased sediment
233 flux due to mass movement.

234 The regolith thickness, h [L] of a soil-mantled hillslope can be derived by calculating
235 the difference between the elevation of the ground surface, Z_s [L] and the underlying

236 topography, Z_b [L] of the fresh bedrock

$$237 \quad h(x, y) = Z_s(x, y) - Z_b(x, y), \quad (1)$$

238 where the coordinates (x, y) are used to denote spatial location. Spatial maps of Z_s are
239 readily available from digital elevation models (DEMs), yet the topography of the fresh
240 bedrock, Z_b is largely unknown as the interior of a hillslope is very difficult and costly
241 to access. Relatively few publications can be found in the geomorphologic literature that
242 have documented directly the depth to the fresh bedrock underlying ridge and valley
243 topography [*Ruxton and Berry*, 1959; *Thomas*, 1966]. Those studies that have mapped
244 Z_b have illuminated that the weathered zone is thickest at the ridge top and to get pro-
245 gressively thinner downslope [*Ruxton and Berry*, 1959; *Thomas*, 1966; *Ruddock*, 1967;
246 *Feininger*, 1971]. What is more, detailed studies of weathering profiles published many
247 decades ago have identified that groundwater can impede chemical weathering thereby re-
248 stricting the depth of the weathered zone [*Ruxton and Berry*, 1959; *Thomas*, 1966]. These
249 early experimental findings, have stimulated *Rempe and Dietrich* [2014] to suggest a new
250 hypothesis for rock mass weathering underlying soil-mantled hillslopes. This hypothesis
251 assumes that the groundwater exerts a bottom-up control on fresh bedrock topography,
252 and explains published experimental findings of progressively thinner weathered zones
253 downslope. This hypothesis is diametrically opposed to the classic top-down hypothesis
254 that is used by many soil depth models. The top-down hypothesis links the soil thick-
255 ness to processes taking place at the ground surface by assuming that the thickness of
256 the weathered zone is set by the relative rates of erosion and the soil production in the
257 weathering front.

258 The bedrock depth model of *Rempe and Dietrich* [2014] builds on the one-dimensional,
 259 steady-state form of the Boussinesq equation for groundwater flow [*Bear*, 2013]

$$260 \quad \frac{1}{2}K \frac{\partial^2 Z_b^2}{\partial x^2} + \phi C_o = 0, \quad (2)$$

261 where K [LT^{-1}] denotes the saturated hydraulic conductivity of the bedrock, x [L] is the
 262 horizontal distance from the ridge, ϕ [-] signifies the saturated drainable pore space of the
 263 bedrock (= porosity), and C_o [LT^{-1}] represents the channel incision rate at the base of the
 264 hillslope. By assuming strictly horizontal flow, topographic symmetry about the ridge,
 265 and a channel elevation at the bottom of the hillslope, the following closed-form equation
 266 can be derived for the elevation of the transition from fresh to weathered bedrock

$$267 \quad Z_b(x) = \sqrt{\frac{\phi C_o}{K}(L^2 - x^2)}, \quad (3)$$

268 where L [L] is the hillslope length, and the term $(L^2 - x^2)$ can be interpreted as distance to
 269 the drainage channel. A step-by-step derivation of Equation (3) is given in the supporting
 270 information of *Rempe and Dietrich* [2014], and thus will not be repeated herein. Equation
 271 (3) predicts that the depth of the weathered zone decreases from the hilltop to the valley
 272 floor with convexity and depth of the bedrock surface determined by the parameters ϕ ,
 273 C_o , K .

274 Our DTB model uses as basic building block the analytic solution of Equation (3) but
 275 includes two important extensions that enhance applicability of the model to watersheds
 276 with convex and/or concave bedrock surfaces underneath the drainage valley and thin
 277 weathered zones and/or exposed rock on steep hillslopes subject to mass movement. This
 278 DTB model solves for the bedrock depth at two spatial coordinates, x and y and con-
 279 tains two new variables, Ψ and Λ whose values are derived from the slope angle and

280 drainage distance, respectively, and three additional (quasi)-physical parameters. The
 281 basic formulation of the DTB model is given by the following closed-form equation

$$282 \quad Z_b(x, y) = \frac{\Psi}{\Lambda} \sqrt{\Phi L_d^2(x, y)}, \quad (4)$$

283 where Ψ [-] measures the effect of mass movement on the bedrock surface, Λ [-] determines
 284 the shape and depth of the bedrock valley, and is hereafter also referred to as the bedrock-
 285 valley shape term, L_d [L] denotes the horizontal distance from the drainage, and $\Phi =$
 286 $\phi C_0/K$ [-] is a scalar that summarizes conveniently the combined effect of rock porosity,
 287 permeability, and the channel incision rate on the elevation of the fresh bedrock, Z_b . The
 288 scalar variables Λ and Ψ are bounded between zero and one and determine the regolith
 289 thickness underneath valleys and steep slopes. The drainage distance, $L_d(x, y)$, of each
 290 spatial location in the watershed is derived from the surface topography using recursive
 291 DEM computation [Tesfa et al., 2009; Catani et al., 2010]. No distinction has to be made
 292 between drainage lines and hillslope lines to predict $Z_b(x, y)$ underneath the watershed.
 293 Thus a single call to Equation (4) suffices to derive the elevation of the bedrock surface
 294 for given (x, y) coordinates.

295 Mass movement is described in analogy with the nonlinear slope-dependent model of
 296 Roering et al. [1999]

$$297 \quad \Psi = 1 - \min [1, (|\nabla Z_s|/S_c)^2], \quad (5)$$

298 where ∇Z_s [-] denotes the slope gradient of the surface topography and S_c [-] signifies the
 299 critical slope angle beyond which mass movement is initiated. We follow Perron [2011],
 300 and calculate the norm $|\nabla Z_s|$ using

$$301 \quad |\nabla Z_s| = \sqrt{Z_{s,x}^2 + Z_{s,y}^2}, \quad (6)$$

302 where $Z_{s,x}$ and $Z_{s,y}$ are the gradients of the slope in the x and y direction, respectively.
 303 Equation (5) predicts regolith loss on hillslopes steeper than the threshold angle S_c . This
 304 movement of mass (due to landslides) gives rise to exposed rock.

305 The variable Λ in Equation (4) determines the hillslope-to-valley transition morphology
 306 and is computed as follows

$$307 \quad \Lambda = \exp \left[- \lambda_1 (1 - \bar{L}_d)^{\lambda_2} \right], \quad (7)$$

308 where \bar{L}_d denotes the normalized drainage distance, and λ_1 and λ_2 are shape parameters
 309 that determine the bedrock shape (curvature) and depth in the valley at the base of the
 310 hillslope. This provides a mechanism to better describe the topographic signature of valley
 311 incision by debris flow and landslides [Tarolli and Fontana, 2009]. Table 1 summarizes
 312 the main variables and parameters of the DTB model. The effects of the variables Ψ and
 313 Λ on the predicted spatial distribution of the regolith thickness is discussed in the next
 314 section.

3. PARAMETER SENSITIVITY ANALYSIS

315 To test the predictive capability of the DTB model, we confront the model with regolith
 316 depth data of a typical hillslope of Rio de Janeiro. We first benchmark the model using
 317 an artificial topographic surface derived from n_s different sine waves

$$318 \quad Z_s(x) = \sum_{i=1}^{n_s} \omega_i \sin(\beta_i x + \chi_i), \quad (8)$$

319 where x [L] is the horizontal distance along the hillslope, and ω , β , and χ are unitless
 320 coefficients that signify the amplitude, frequency, and phase of each individual sine wave.
 321 The synthetic surface topography used herein was derived by setting $n_s = 2$ using values
 322 of the coefficients of Equation (8) listed in Table 2.

323 Figure 1 now presents a sensitivity analysis of the parameters of the DTB model. The
324 four different horizontal panels show the DTB model predicted regolith profiles underneath
325 the artificial hillslope for different values of the parameters Φ (top), λ_1 (top-middle), λ_2
326 (bottom-middle), and S_c (bottom). The artificial topography (surface) of Equation (8)
327 is separately indicated in each plot with the black line. The results of Figure 1 will help
328 build intuition and insights on how the different parameters of the DTB model affect the
329 simulated bedrock surface topography. The landscape elements "hilltop", "sideslope" and
330 "drainage" are used herein to discuss our findings. Their position is indicated in 1A.

331 Before we proceed with the main findings of the sensitivity analysis, we first interpret all
332 the simulated bedrock depth profiles of the DTB model displayed in Figure 1. Regardless
333 of the parameter values used in the DTB model, the weathered zone appears largest at
334 the hilltop and then progressively thins downwards. This profile of the bedrock depth
335 underneath the hillslope is in agreement with field observations of upland and lowland
336 areas [*Liang and Uchida, 2014; Kim et al., 2015*] and mimics qualitatively the output of
337 the *Rempe and Dietrich [2014]* model. The effect of the parameter S_c (regolith movement
338 due to landslides) on the output of the DTB model is shown in Figure 1(G) and (H)
339 and reduces, as expected, the thickness of the weathered zone along the sideslope. The
340 effect of the DTB variable Λ (hillslope-to-valley morphology) is visible in most of the
341 displayed bedrock depth profiles with a shape and curvature of the bedrock surface in the
342 valley (drainage) that deviates considerably from the concave drainage profiles simulated
343 exclusively by Equation (3) of *Rempe and Dietrich [2014]*.

344 We now move on to the results of the sensitivity analysis. The top panel in Figure 1(A)
345 shows that larger values of the parameter Φ increase the thickness of the unweathered

346 zone underneath the hillslope. This increase in bedrock depth is largest at the hilltop
347 (as explained by for instance a high rock permeability), and gets progressively smaller
348 downslope towards the base of the hillslope (drainage). The morphology of the bedrock
349 surface in the valley appears gently convex, but assumes a concave shape when the value
350 of parameter λ_1 is increased from 0.5 to 2 (see Figure 1(B)).

351 The top-middle panel (second from top) of Figure 1 illustrates the effect of λ_1 on the
352 simulated bedrock depth profiles. It is evident that this parameter affects only the bedrock
353 depth topography and curvature in the valley. For $\lambda_1 = 0.5$ in Figure 1(C) and (D), the
354 unweathered zone in the valley (drainage) is really thin and the bedrock surface is almost
355 exposed at the center of the channel. As will be shown in the next panel (bottom-middle)
356 this result is independent on the value of λ_2 . A convex curvature emerges of the bedrock
357 surface below the channel when Ψ is increased from 0.005 in Figure 1(C) to 0.02 in Figure
358 1(D). For larger values of λ_1 the thickness of the unweathered zone increases with a smooth
359 bedrock-valley shape for $\lambda_1 = 1.5$ and V-shape bedrock surface for $\lambda_1 = 2.5$.

360 The bottom-middle panel in Figure 1 displays how parameter λ_2 affects the predicted
361 elevation of the bedrock surface topography. The DTB simulated bedrock depth on the
362 hilltop and sideslope appears insensitive to parameter λ_2 . Indeed, values of λ_2 of 10, 20,
363 and 50 give an exactly similar bedrock elevation underneath the sideslope and hilltop.
364 The same holds true for the thickness of the weathered zone exactly at the mid-point of
365 the drainage channel. The elevation of the fresh bedrock at this lowest point of the surface
366 topography is fixed for different values of λ_2 . Beyond this center-point the bedrock depth
367 varies as function of λ_2 , the extent to which depends on the value of λ_1 . As is evident
368 from Figure 1(E), for relatively low values of λ_1 the bedrock topography simulated by the

369 DTB model does not depend on λ_2 . However, this sensitivity of the DTB model output to
370 λ_2 increases for larger values of λ_1 . Indeed, Figure 1(F) shows an increasingly V-shaped
371 morphology of the bedrock surface underneath the drainage valley. The results presented
372 herein demonstrate that the shape and depth of the bedrock surface underneath the valley
373 is determined by parameters λ_1 and λ_2 and thus the value of Λ in Equation (4) of the
374 DTB model. The elevation and curvature of the bedrock surface in the valley might be
375 explained by the horizontal stress field [*Clair et al.*, 2015].

376 The bottom panel in Figure 1 shows the effect of S_c on the simulated regolith profiles.
377 The effect of mass movement is most noticeable for the bedrock topography underneath
378 the sideslope as the depth of the weathered zone at the hilltop and the drainage valley
379 appear unaffected. The larger the value of the critical slope angle, the more unlikely mass
380 movement will take place, and thus the more similar the DTB model simulated depth to
381 bedrock underneath the slope. Indeed, the bedrock profiles for $S_c = 1$ and $S_c = 1.3$ are in
382 excellent agreement and follow closely the shape of the topographic surface. For smaller
383 values of S_c , however the slope angle simulated by the DTB model approaches a critical
384 threshold of about 27° and the thickness of the weathered zone beneath the hillslope
385 decreases considerably. This is readily visible in Figure 1(H) (dotted red line). The
386 thickness of the regolith has decreased substantially in the steepest part of the hillslope just
387 below the hilltop, and the weathered zone approaches an approximately fixed depth from
388 the inflection point downwards towards the drainage valley. This trend is in agreement
389 with our field knowledge from hillslopes in Rio de Janeiro, Brazil. We therefore posit that
390 our DTB model can be used for hillslopes with steep gradients whose underlying fresh-
391 bedrock surface is determined by rock properties (low values of Φ in Fig.1(G)) and surface

steeping (Fig.1(H)). Note that for $S_c = 0.65$ the DTB model predicts a rather peculiar
bedrock depth at the sideslope. At this point, it is not clear whether this constitutes a
structural limitation (epistemic error) of Equation (4) or whether this highlights an issue
with the parameter values.

In summary, the parameter Φ (rock properties) determines the depth to bedrock un-
derneath the hillslope and hilltop. The parameter S_c (critical slope angle) can activate
the process of mass movement (if set sufficiently small) and this affects the angle of the
bedrock surface and depth of the regolith beneath the sideslope. The parameters λ_1
and λ_2 determine the shape (convex/concave) and depth of the bedrock surface in the
drainage valley. With these four fitting parameters the DTB model as proposed herein,
can simulate the bedrock surface of convergent and divergent hillslopes.

A final remark about the results of the sensitive analysis is appropriate. The bedrock
depths shown in Figure 1 suggest that the parameters λ_1 and λ_2 , as they appear in
Equation (7), might be correlated as they both determine the topography of the valley-
bedrock surface. We will revisit this issue of parameter identifiability (and lack thereof) in
section 5.1 of this paper. We are now left with a treatment of the DTB model parameters.
Their values are catchment (hillslope)-dependent and need to be derived by fitting the
model against spatially distributed observations of DTB.

4. INVERSE MODELING

The DBT model contains several coefficients that are difficult to be measured directly in
the field at the application scale of interest, and thus have to be determined by calibration
instead using some spatially distributed map of regolith depth observations. If we denote

413 with \mathcal{F} Equation (4) then we can write our DTB model as follows

$$414 \quad \mathbf{H} \leftarrow \mathcal{F}(\boldsymbol{\theta}, \nabla Z_s, \mathbf{L}_d) + \mathbf{e}, \quad (9)$$

415 where $\mathbf{H} = \{h_1, \dots, h_n\}$ is a n -vector of simulated bedrock depths at spatial coordi-
 416 nates, $(x_1, y_1) \dots (x_n, y_n)$, $\boldsymbol{\theta} = \{\Phi, \lambda_1, \lambda_2, S_c\}$ signifies the d -vector of model parameters,
 417 $\mathbf{L}_d = \{L_d(x_1, y_1), \dots, L_d(x_n, y_n)\}$ stores the n -values of the drainage distance of each
 418 measurement location, and $\mathbf{e} = \{e_1, \dots, e_n\}$ represents the vector of observation errors.
 419 The vector \mathbf{e} includes observation error as well as error due to the fact that the DTB
 420 model, $\mathcal{F}(\cdot)$ may be systematically different from reality, $\mathfrak{S}(\boldsymbol{\theta})$ for the parameters $\boldsymbol{\theta}$. The
 421 latter may arise from an improper model formulation (epistemic errors) and topographic
 422 uncertainty (due to DEM measurement errors and/or inadequate resolution).

423 If we adopt a Bayesian formalism then we can derive the posterior distribution of the
 424 parameters, $p(\boldsymbol{\theta}|\tilde{\mathbf{H}})$, by conditioning the spatial behavior of the model on the n -measured
 425 values of the bedrock depth, $\tilde{\mathbf{H}} = \{\tilde{h}_1, \dots, \tilde{h}_n\}$ using

$$426 \quad p(\boldsymbol{\theta}|\tilde{\mathbf{H}}) = \frac{p(\boldsymbol{\theta})p(\tilde{\mathbf{H}}|\boldsymbol{\theta})}{p(\tilde{\mathbf{H}})}, \quad (10)$$

427 where $p(\boldsymbol{\theta})$ is the prior parameter distribution, $L(\boldsymbol{\theta}|\tilde{\mathbf{H}}) \equiv p(\tilde{\mathbf{H}}|\boldsymbol{\theta})$ denotes the likelihood
 428 function, and $p(\tilde{\mathbf{H}})$ signifies the evidence. This latter variable is a constant that is inde-
 429 pendent of the parameter values and acts as a normalization constant (scalar) so that the
 430 posterior distribution integrates to unity

$$431 \quad p(\tilde{\mathbf{H}}) = \int_{\Theta} p(\boldsymbol{\theta})p(\tilde{\mathbf{H}}|\boldsymbol{\theta})d\boldsymbol{\theta} = \int_{\Theta} p(\boldsymbol{\theta}, \tilde{\mathbf{H}})d\boldsymbol{\theta}, \quad (11)$$

over the parameter space, $\boldsymbol{\theta} \in \Theta \in \mathbb{R}^d$. In practice, $p(\tilde{\mathbf{H}})$ is not required for posterior
 estimation as all statistical inferences about $p(\boldsymbol{\theta}|\tilde{\mathbf{H}})$ can be made from the unnormalized

density

$$p(\boldsymbol{\theta}|\tilde{\mathbf{H}}) \propto p(\boldsymbol{\theta})L(\boldsymbol{\theta}|\tilde{\mathbf{H}}). \quad (12)$$

432 We conveniently assume that the prior distribution, $p(\boldsymbol{\theta})$ is uniform, $p(\boldsymbol{\theta}) \propto c$, where c is
 433 a constant. This means that we a-priori do not favor any values of the model parameters,
 434 and instead use uniform prior ranges. The main culprit now resides in the definition
 435 of the likelihood function, $L(\boldsymbol{\theta}|\tilde{\mathbf{H}})$, used to summarize the distance between the model
 436 simulations, $\mathbf{H}(\boldsymbol{\theta})$, and corresponding observations, $\tilde{\mathbf{H}}$. If we assume the error residuals of
 437 the observed and simulated bedrock depths to be normally distributed and uncorrelated,
 438 then the likelihood function can be written as

$$439 \quad L(\boldsymbol{\theta}|\tilde{\mathbf{H}}) = \prod_{i=1}^n \frac{1}{\sqrt{2\pi\hat{\sigma}_i^2}} \exp \left[-\frac{1}{2} \left(\frac{\tilde{h}_i - h_i(\boldsymbol{\theta})}{\hat{\sigma}_i} \right)^2 \right], \quad (13)$$

440 where $\hat{\sigma}_i$ is an estimate of the standard deviation of the measurement error of the
 441 i th soil depth observation. This formulation allows for homoscedastic (constant vari-
 442 ance) and heteroscedastic measurement errors (variance dependent on magnitude of each
 443 data point). If homoscedasticity is expected and the variance of the error residuals,
 444 $s^2 = \frac{1}{n-1} \sum_{t=1}^n (e_t(\mathbf{x}))^2$ is taken as sufficient statistic for σ^2 , then one can show that the
 445 likelihood function simplifies to

$$446 \quad L(\boldsymbol{\theta}|\tilde{\mathbf{H}}) \propto \sum_{i=1}^n |\tilde{h}_i - h_i(\boldsymbol{\theta})|^{-n}. \quad (14)$$

447 Once the prior distribution and likelihood function have been defined, what is left in
 448 Bayesian analysis is to summarize the posterior distribution. For models such as Equation
 449 (4) which is nonlinear in its parameters, the posterior distribution $p(\boldsymbol{\theta}|\tilde{\mathbf{H}})$ cannot be
 450 obtained by analytic means nor by analytic approximation. We therefore resort to iterative
 451 methods that approximate the posterior probability density function by generating a large

452 sample from this distribution. The most powerful of such sampling methods is Markov
 453 chain Monte Carlo (MCMC) simulation using the Metropolis algorithm [*Metropolis et al.*,
 454 1953]. The basis of MCMC simulation is a Markov chain that generates a random walk
 455 through the search space and successively visits solutions with stable frequencies stemming
 456 from a stationary distribution, $\bar{\pi}(\cdot)$. To explore the target distribution, $\bar{\pi}(\cdot)$, a MCMC
 457 algorithm alternates between three basic steps. First, a proposal $\boldsymbol{\theta}_p$ is generated from the
 458 current state of the Markov chain, $\boldsymbol{\theta}_t$ using some jumping distribution, $q(\boldsymbol{\theta}_t \rightarrow \boldsymbol{\theta}_p)$. Next,
 459 this proposal is accepted with Metropolis probability

$$460 \quad P_{\text{acc}}(\boldsymbol{\theta}_t \rightarrow \boldsymbol{\theta}_p) = \min \left[1, \frac{p(\boldsymbol{\theta}_p)q(\boldsymbol{\theta}_p \rightarrow \boldsymbol{\theta}_t)}{p(\boldsymbol{\theta}_t)q(\boldsymbol{\theta}_t \rightarrow \boldsymbol{\theta}_p)} \right]. \quad (15)$$

461 Finally, if the proposal is accepted, the chain moves to $\boldsymbol{\theta}_p$, and thus $\boldsymbol{\theta}_{t+1} = \boldsymbol{\theta}_p$, other-
 462 wise the current position is retained, $\boldsymbol{\theta}_{t+1} = \boldsymbol{\theta}_t$. Repeated application of these three steps
 463 results in a Markov chain which, under certain regularity conditions, has a unique station-
 464 ary distribution with posterior probability density function, $\bar{\pi}(\cdot)$. In practice, this means
 465 that if one looks at the values of $\boldsymbol{\theta}$ sufficiently far from the arbitrary initial value, that is,
 466 after a burn-in period, the successively generated states of the chain will be distributed
 467 according to $\bar{\pi}(\cdot)$, the d -dimensional posterior probability distribution of $\boldsymbol{\theta}$. Burn-in is
 468 required to allow the chain to explore the search space and reach its stationary regime.

469 If a symmetric jumping distribution is used, that is $q(\boldsymbol{\theta}_t \rightarrow \boldsymbol{\theta}_p) = q(\boldsymbol{\theta}_p \rightarrow \boldsymbol{\theta}_t)$, then
 470 Equation (15) simplifies to

$$471 \quad P_{\text{acc}}(\boldsymbol{\theta}_t \rightarrow \boldsymbol{\theta}_p) = \min \left[1, \frac{p(\boldsymbol{\theta}_p)}{p(\boldsymbol{\theta}_t)} \right]. \quad (16)$$

472 This selection rule has become the basic building block of the random walk Metropolis
 473 (RWM) algorithm, the earliest MCMC method. This RWM algorithm can be coded in

474 just a few lines and requires only a jumping distribution, a function to generate uniform
475 random numbers, and a function to calculate the probability density of each proposal,
476 which is simply equivalent to the product of the prior distribution and likelihood function
477 of Equation (14).

478 The efficiency of the RWM algorithm is determined by the choice of the proposal dis-
479 tribution, $q(\cdot)$ used to create trial moves (transitions) in the Markov chain. When the
480 proposal distribution is too wide, too many candidate points are rejected, and therefore
481 the chain will not mix efficiently and converge only slowly to the target distribution. On
482 the other hand, when the proposal distribution is too narrow, nearly all candidate points
483 are accepted, but the distance moved is so small that it will take a prohibitively large num-
484 ber of updates before the sampler has converged to the target distribution. The choice of
485 the proposal distribution is therefore crucial and determines the practical applicability of
486 MCMC simulation in many fields of study [Vrugt, 2016].

487 In this paper, MCMC simulation of the DTB model has been performed using the
488 DREAM algorithm [Vrugt *et al.*, 2008, 2009]. This multi-chain MCMC simulation algo-
489 rithm automatically tunes the scale and orientation of the proposal distribution, $q(\cdot)$ en
490 route to the target distribution. This is one of the reasons DREAM exhibits excellent
491 sampling efficiencies on complex, high-dimensional, and multi-modal target distributions.
492 The use of multiple chains offers a robust protection against premature convergence, and
493 opens up the use of a wide arsenal of statistical measures to test whether convergence to
494 the posterior distribution has been achieved. We evaluate the DTB model using lumped
495 and spatially distributed parameter values. These values are stored in the d -vector θ .

5. BAYESIAN INFERENCE WITH DREAM: SYNTHETIC DATA

496 We now proceed with fitting of the DTB model parameters using Bayesian inference
 497 with DREAM. To be able to benchmark our findings we start with a synthetic record of
 498 regolith depth observations created on a regular DEM. This DEM is presented in Figure
 499 2 and simply copies Equation (8) to the y -direction of the xy plane using 100 different
 500 replicates of the topographic surface with $\Delta y = 2$. This DEM is now sampled at random
 501 100 different times (see black dots in Fig. 2(A)) and the regolith depth at each sampled
 502 (x, y) location of the grid is computed using

$$503 \quad \tilde{h}(x, y) = Z_s(x, y) - \alpha_1 [\alpha_2 + L_d(x, y) / \max(L_d)]^2 + \epsilon_m, \quad (17)$$

504 where $Z_s(x, y)$ [L] is the elevation of the surface topography at spatial coordinates x, y ,
 505 and α_1 [L] and α_2 [-] are two coefficients whose values determine the borehole depth, and
 506 ϵ_m [L] denotes the measurement data error of the bedrock depth data. Thus, the regolith
 507 depth at any location in the DEM is computed by subtracting from the surface elevation
 508 the borehole depth and adding a measurement error.

509 We assume that $\alpha_1 = 8$ and $\alpha_2 = 0.1$ and draw the measurement data error from a
 510 normal distribution with $a = 0$ mean and standard deviation $b = 1/2\hat{\sigma}_{Z_b}$, or $\epsilon_m \sim \mathcal{N}(a, b)$,
 511 where $\hat{\sigma}_{Z_b}$ denotes the standard deviation of the $n = 100$ bedrock depth observations
 512 before their corruption with a measurement error. Table 3 summarizes the statistical
 513 properties of the resulting bedrock depth data set, including sample size and the minimum,
 514 maximum, mean and standard deviation of the regolith thickness. This latter statistic
 515 determines the measurement error of the bedrock depth observations, $\hat{\sigma}_{Z_b} = 1.43$ [m] and
 516 provides a benchmark of the "best-fit" attainable by the DTB model (of which more later).
 517 The final data set of bedrock depth observations is stored in the n -vector $\tilde{\mathbf{H}} = \{\tilde{h}_1, \dots, \tilde{h}_n\}$

518 and is now used to calibrate the DTB model using lumped and spatially distributed
 519 parameter values.

5.1. DTB Model with Lumped Parameter Values

520 The DTB model has four parameters $\boldsymbol{\theta} = \{\Phi, \lambda_1, \lambda_2, S_c\}$ whose values are difficult to
 521 be measured directly in the field and hence require calibration against observed bedrock
 522 depth data. In the absence of detailed geologic data, we conveniently hypothesize the
 523 underlying rock mass to be homogeneous and use spatially invariant values of the DTB
 524 parameters, $\boldsymbol{\theta}$. We will revisit this hypothesis in the next section of this paper using
 525 spatially distributed parameter values. We adopt the likelihood function of Equation
 526 (14) and use a multivariate uniform prior distribution for the DTB model parameters.
 527 With such noninformative prior, the posterior density in Equation (16) is then simply
 528 proportional to Equation (14) and used herein for inference of the DTB model parameters.
 529 The prior ranges of the parameters are listed in Table 4. The minimum and maximum
 530 value of parameter Φ are set to 10^{-4} and 10^{-1} , respectively. These ranges are rather
 531 wide, and with a bedrock porosity of $\phi = 0.1$ and values for the hydraulic conductivity
 532 of consolidated crystalline rocks that range between 10^{-8} and 10^{-13} m/s, gives values of
 533 the channel incision rate, C_o of 0.03 to 3 mm/year. These ranges of C_o are in agreement
 534 with values reported in *Rempe and Dietrich* [2014]. The prior ranges of $\lambda_1 \in [0.1, 3]$ and
 535 $\lambda_2 \in [1, 20]$ are derived from the results of section 3, and the bounds of $S_c \in [0.8, 1.5]$ are
 536 inspired from the literature.

537 Figure 3 presents a scatter plot matrix of the posterior samples derived with the DREAM
 538 algorithm. The main diagonal displays histograms of the marginal distribution of each
 539 individual DTB model parameter, whereas the off-diagonal graphs display bivariate scat-

540 ter plots of the posterior samples. The x -axes matches exactly the prior ranges of the
541 parameters (except for the parameter Φ) and the maximum a-posteriori (MAP) solution
542 is separately indicated in each histogram with the blue cross. These parameter values are
543 associated with the highest value of the likelihood function of Equation (14) of all pos-
544 terior samples generated by DREAM, and this MAP solution coincides almost perfectly
545 with the posterior median values.

546 The posterior histogram of the DTB model parameter Φ centers nicely around its MAP
547 solution and follows an approximately normal distribution. The marginal distribution of
548 this parameter occupies a (very) small portion of its uniform prior distribution, which
549 demonstrates that this parameter is very well defined by calibration against the observed
550 (synthetic) bedrock depth data. The posterior histograms of the two bedrock-valley shape
551 parameters, λ_1 and λ_2 are not particularly well identifiable. The marginal distribution
552 of λ_1 in Figure 3(F) exhibits normality, although the histogram is somewhat skewed to
553 the left and occupies a large part of the prior distribution. The MAP solution of λ_1
554 between 1 and 2 indicates that the bedrock surface in the valley does not reach the
555 ground surface (see Figure 1). In other words, the valley is mantled with a thin layer
556 of soil. The marginal distribution of parameter λ_2 deviates considerably from normality
557 and is much better described with an uniform distribution. Note that the histogram of
558 λ_2 appears truncated at the upper end by its prior distribution. As the probability mass
559 is distributed mainly at higher values of λ_2 , we conclude that the shape of the bedrock
560 surface in the valley follows closely that of the surface topography in the channel. The
561 parameter S_c follows a log-normal distribution and is truncated at the lower boundary
562 of its prior distribution. That relatively low values of S_c are perhaps not that surprising

563 as the artificially generated bedrock depth observations were made close to the ground
564 surface in a relatively steep hillslope. We will revisit the posterior distribution of S_c later
565 in this paper. The bivariate scatter (off-diagonal) plots highlight negligible the presence of
566 some correlation between the DTB parameters. For instance, consider the (Ψ, S_c) scatter
567 plots (top right, bottom left) which depicts a somewhat nonlinear dependency between
568 these two parameters.

569 The performance of the DTB model is now evaluated using two statistical metrics
570 including the the root mean squared error (RMSE) and the Pearson product moment
571 correlation coefficient, or ρ -statistic. Mathematical formulaes for both are readily found
572 in statistics textbooks. The RMSE measures the average distance between the observed
573 and simulated bedrock depth data. This statistic has a similar unit as the observations
574 themselves. The lower the value of the RMSE the closer the model predictions to the data.
575 The ρ -statistic measures the strength and direction of a linear relationship between two
576 variables. It is used herein to quantify how well the DTB model predicted bedrock depths
577 fall on the (1:1) line with their observed values. Table 5 summarizes the performance of
578 the DTB model using the posterior mean parameter values. The calibrated DTB model
579 has a ρ -value of 0.86 and RMSE of approximately 1.52 m. This value of the RMSE is
580 much lower than that derived from an uncalibrated DTB model (not shown) and of similar
581 magnitude as the measurement data error, $\hat{\sigma} = 1.43$ m. This latter finding is particularly
582 important and demonstrates the ability of the DTB model to describe accurately the
583 observed bedrock depth data with spatially invariant parameter values.

584 The assumption of parameter homogeneity is convenient but might not be borne out
585 by the actual properties of the hillslope or watershed which can exhibit significant system

586 heterogeneities at different spatial scales. Much effort would be required to characterize
 587 adequately the rock mass properties such as discontinuities, saturated permeability and
 588 porosity for a reasonably sized watershed. The use of spatially distributed parameter
 589 values provides a means to account implicitly, and in a relatively simple way, for system
 590 heterogeneities that are difficult, or sometimes impossible, to characterize adequately in
 591 the field. For example, if the value of the parameter Φ is varied spatially, then the DTB
 592 model will assume spatially varying permeability and/or porosity values, given measured
 593 values of the channel-incision rate, C_o .

594 In the next section of this paper, we will investigate the benefits of using a distributed
 595 DTB parameterization. This distributed approach is of particular relevance to real-world
 596 data sets, but cannot be expected a-priori to improve significantly upon the fitting results
 597 of our lumped DTB parameterization for the synthetic data set which already achieved
 598 posterior RMSE values close to the measurement data error. Any further improvements
 599 in quality of fit of the DTB model must be carefully interpreted.

5.2. DTB Model with Spatially Distributed Parameter Values

600 The use of a distributed parameterization requires some changes to the setup of the
 601 DTB model. This is depicted schematically in Figure 4 which summarizes the setup of
 602 the DTB model for an invariant (lumped) and variant (distributed) parametrization. The
 603 top panel displays the surface of an idealized DEM consisting of P cells (pixels). To
 604 simplify notation we use a single variable, $i = \{1, \dots, P\}$ to denote the xy coordinates
 605 of a DEM cell. The input data of the DTB model in Equation (4) differs per grid cell
 606 and is stored in the vector, $\mathbf{U}_i = \{\nabla Z_{bi}, L_{di}\}$. If a lumped parameterization of the
 607 DTB model is used then it suffices to use the same parameter values, $\boldsymbol{\theta} = \{\Phi, \lambda_1, \lambda_2, S_c\}$

608 for each cell of the xy grid. This approach is most convenient and widespread in the
609 geomorphologic literature. A distributed DTB parameterization uses different parameter
610 values for each region of the DEM. This approach increases significantly the dimensionality
611 of the parameter estimation problem and the required CPU-time for DTB calibration.
612 Also, the spatially distributed framework requires the user to define a spatial pattern for
613 each of the model parameters. For example, in Figure 4 we assume a simple block pattern
614 of $r = 16$ equal-sized squares for each of the parameters. Each individual square thus
615 consists of four different grid cells. In a distributed parameterization, the values of the
616 parameters of the first square (top left) are thus assigned to grid cells 1, 2, 9 and 10.
617 After the parameterization of the DTB model has been defined, the DREAM algorithm
618 proceeds with statistical inference of the model parameters using distributed observations
619 of the bedrock depth. Both implementations use the same source code of the DTB model
620 but differ in their assignment of the parameter values.

621 We are now left with the question of how to distribute the values of Φ , λ_1 , λ_2 and S_c over
622 the grid domain of interest. Care should be exercised not to use too many parameters in
623 lieu of overfitting. Two main approaches can be used to determine the spatial distribution
624 of the parameter values. The first approach fixes a-priori the spatial structure of the
625 parameters and then determines the actual values of this pattern by fitting the DTB
626 model to the observed bedrock depth data. An example of this approach is found in Fig.
627 2(B) for a block pattern and this design is used herein for illustrative purposes. One
628 can also link the spatial structure of θ to properties of the DEM to guide the spatial
629 structure of the parameter values. The topographic position index [*Tesfa et al.*, 2009;
630 *Reu et al.*, 2013] can be used as guiding metric to determine the spatial structure of the

631 parameters. This approach fixes a-priori the spatial structure of the DTB parameters, and
632 this pattern might therefore not necessarily honor the underlying bedrock heterogeneity.
633 Alternatively, one can use so-called model-reduction techniques and let the actual regolith
634 depth observations determine simultaneously the pattern and values of the DTB model
635 parameters. Examples of such model-reduction approaches include the discrete cosine
636 transform [*Linde and Vrugt, 2013; Lochbühler et al., 2015*], wavelet transform [*Davis and*
637 *Li, 2011; Jafarpour, 2011*], and singular value decomposition [*Laloy et al., 2012; Oware et*
638 *al., 2013*]. We have tested this alternative approach in the present study but found little
639 improvements in the quality of fit of the DTB model (not shown).

640 We now illustrate the results of the DTB model using two different distributed pa-
641 rameterizations of Φ . In our first trial, we divide the xy plane of the DEM into $r = 4$
642 equal-sized rectangles and assume a different value of Φ for each oblong. The remaining
643 parameters (λ_1 , λ_2 and S_c) continue to take on a single lumped value that pertains to
644 the entire spatial domain (Figure 4). The parameter dimensionality has increased from
645 $d = 4$ in the first case study to $d = 7$ in the present study. In the second trial, we increase
646 the number of square blocks for the parameter Φ to 25 as shown in Figure 2(B). This
647 then leaves us with a total of $d = 28$ parameter values that require calibration against the
648 observed bedrock depth data using the DREAM algorithm.

649 Figure 5 displays trace plots of the \hat{R} -statistic of *Gelman and Rubin* [1992] for each
650 of the model parameters ($d = 28$) using the last 50% of the samples stored in each of
651 the $N = 15$ Markov chains. This convergence diagnostic compares the within-chain and
652 between-chain variance of each parameter $j = \{1, \dots, d\}$ of the DTB model. The different
653 parameters are color coded. Convergence to a stationary distribution can be declared if

654 the \hat{R}_j -statistic of each of the $d = 28$ parameters drops below the critical value of 1.2.
 655 Results demonstrate that about 50,000 DTB model evaluations are required for DREAM
 656 to converge successfully to a stationary distribution and satisfy the convergence threshold.
 657 This rather large number of model evaluations involves a rather low computational effort
 658 due to the relative CPU-efficiency of the DTB model. If desired, each Markov chain
 659 sampled with DREAM can be evaluated on a different processor permitting inference of
 660 CPU-demanding transient models. Most of the DTB parameters appear well defined by
 661 calibration to the observed bedrock depth data (not shown). We will investigate this
 662 further in the next section of this paper using real-world observations of the depth to
 663 bedrock.

664 To determine which of the model complexities is best supported by the available regolith
 665 depth data we use Akaike's Information Criterion (AIC) [Akaike, 1974]. This metric takes
 666 into consideration model complexity (= parameter dimensionality) and the goodness of
 667 fit. Hence, AIC provides a means for model selection. The value of AIC is computed as
 668 follows

$$669 \quad \text{AIC} = -2 \ln\{L(\boldsymbol{\theta}_{\text{MAP}}|\tilde{\mathbf{H}})\} + 2d, \quad (18)$$

670 where $L(\boldsymbol{\theta}_{\text{MAP}}|\tilde{\mathbf{H}})$ is the maximum value of the likelihood function derived from the MAP
 671 (= best) parameter values. Given a collection of models for the data, AIC estimates the
 672 quality of each model, relative to each of the other models. Models with lower AIC values
 673 are preferred statistically. Note, AIC does not give a warning if all models fit poorly, and
 674 hence this metric has to be interpreted jointly with other model performance criteria.

675 Table 5 summarizes the performance of the DTB model with a distributed parameteri-
 676 zation of Φ . The RMSE has reduced from 1.52 (lumped: $d = 4$) to 1.47 m (distributed:

677 $d = 7$) and the ρ -statistic has slightly increased from 0.86 to 0.87. The results of the
678 second trial ($d = 28$) show a further reduction of the RMSE and another increase of the
679 ρ -statistic. In fact, the RMSE is now slightly lower than the (Gaussian) measurement
680 error of $\hat{\sigma}_{Z_b} = 1.43$ used to corrupt the $n = 100$ bedrock depth observations.

681 To understand whether these improvements in fit are statistically warranted, we also
682 list, in the last column of Table 5, the AIC values for each of the three DTB model
683 parameterizations. The lowest value of the AIC is found for the first distributed parameter
684 case with $d = 7$. This constitutes a marginal improvement over the value of $AIC = 192.30$
685 for the lumped parameterization with $d = 4$. This suggest that Φ is better characterized
686 with the use of spatially distributed values. The second distributed case with $d = 28$
687 parameters, albeit having the lowest value of the RMSE and highest ρ -statistic, has a
688 value of $AIC = 221.43$ which is much larger than the other two model parameterizations.
689 These results caution against the use of an excessive number of parameters due to potential
690 problems of overfitting. Indeed, a lumped or a spatially distributed parameterization ($d =$
691 7) of the DTB model suffices for this synthetic data set, and any further improvements
692 in fit are not warranted by the available bedrock depth observations.

693 Thus far, we have focused our attention on the posterior parameter distributions of the
694 DTB model and summary statistics of the quality of fit of the mean solution. We now
695 turn our attention to the simulated output of the DTB model and plot in Figure 6 the
696 bedrock surface of the posterior mean solution of the lumped (solid red) and distributed
697 (dashed red) parameterization for a synthetic hillslope transect. The dark and light gray
698 regions display the 95% prediction uncertainty ranges of the simulated bedrock depths
699 using lumped ($d = 4$) and distributed ($d = 7$) parameter values, respectively. The to-

700 pographic surface is indicated with the black line, and the observed regolith depth data
701 are separately indicated with the solid blue dots. The posterior mean simulation of the
702 lumped and distributed parameter case appears rather similar (as expected from Table
703 5) and tracks closely the observed bedrock depth data. The simulated bedrock surface
704 is much smoother than expected from the observed data and does not fit the malicious
705 small-scale variations of the regolith thickness induced by the measurement error. These
706 erroneous small-scale variations in the bedrock depth appear to be largest at the sideslope,
707 generating a thin regolith thickness in this region. This might explain why the marginal
708 distribution of S_c in Figure 3(P) favors relatively small values. The prediction uncer-
709 tainty of the lumped DTB calibration is much smaller than its counterpart derived from
710 a distributed parametrization, except at the drainage channel. This is a common finding
711 and highlights a trade-off between model complexity (=parameter dimensionality) and
712 prediction uncertainty. We will discuss later the implications of this bedrock prediction
713 uncertainty on hydrologic and geotechnical analysis.

6. BAYESIAN INFERENCE WITH DREAM: APPLICATION TO THE PAPAGAIO RIVER BASIN

714 We now apply the DTB model to a real-world data set. In the next sections we de-
715 scribe the experimental field site, data collection and present the results of DTB model
716 calibration and evaluation for a lumped and distributed parameter case.

6.1. Experimental Field Site

717 Field investigations were carried out in two adjacent watersheds in the Papagaio river
718 basin in Rio de Janeiro, Brazil. These two watersheds have been studied extensively by
719 many different authors in the literature after mass movement occurred in 1996 [*Guimarães*

720 *et al.*, 2003; *Fernandes et al.*, 2004; *Vieira and Fernandes*, 2004; *Gomes et al.*, 2008, 2013]
721 (among others). A detailed description of the field site appears in these cited publications,
722 and thus will not be repeated herein. The geographic location of the field sites is depicted
723 with a red cross in Figure 7 which also presents (left hand side) the topography of the two
724 experimental basins. The white dots signify the measurement locations, and the hillslope
725 transects **AA'** and **BB'** are of particular interest herein. The elevation in the surveyed
726 region ranges between 190 and 360 meters above sea level with slopes that vary between
727 0 to 57°.

728 The local bedrock consists of high-grade metamorphic rocks (Archer gneiss is most
729 frequent) with granite intrusions of coarse-medium granular texture [*Fernandes et al.*,
730 2004; *Vieira and Fernandes*, 2004]. Human impact in the region has been limited to a
731 few small areas used for agricultural activities [*Gomes et al.*, 2008] and the vegetation
732 (Atlantic forest) has been preserved in most parts of the basin. DTB observations were
733 made at $n = 137$ different locations in the two watersheds using a light dynamic cone
734 penetrometer. These locations were carefully selected to maximize information retrieval
735 about the underlying bedrock surface and include a rich sample of convex, concave, planar,
736 convergent and divergent slopes. Statistical properties of the regolith depth observations
737 are listed in Table 3.

738 The smallest of the two experimental watersheds was used primarily to study small-
739 scale variations in the depth to bedrock. This requires the use of neighboring boreholes
740 that measure DTB within a few meters of each other. The southerly and larger watershed
741 was populated more uniformly with different boreholes to investigate more deeply the
742 bedrock surface along a hillslope. This difference in objective is readily apparent in the

743 areal view of the two catchments in Fig. 7. The borehole pattern of the larger watershed
 744 in the south appears much more uniform and organized than its counterpart from the
 745 northerly watershed (left), which contains many more adjacent boreholes. A differential
 746 GPS system was used to determine as accurately and consistently as possible the $\{x, y, z\}$
 747 location of each borehole. We estimate the remaining location error to be on the order of
 748 0.5 m for all the $n = 137$ different boreholes.

6.2. Model Input Data

749 The topographic surface is one of the most important input variables of the DTB model.
 750 Some correction of this surface is usually required to remove small-scale imperfections
 751 arising from (among others) three throw, animal burrows, and LiDAR measurement errors
 752 [*Pelletier and Rasmussen, 2009*]. Such DEM errors can otherwise corrupt the results of
 753 models which rely heavily on the first and second-order derivative of the topography (slope
 754 and curvature of DEM) in their calculation of the soil/bedrock depths. Indeed, when a
 755 DEM is differentiated, the small-scale variability of the topographic data is amplified
 756 relative to large-scale topographic variations that define the overall shape of the hillslope.

757 Even the most accurate and advanced topographic surveying methods such as high
 758 resolution LiDAR exhibit measurement errors that can introduce small-scale defects in the
 759 DEM and deteriorate the simulated bedrock depths by introducing erratic and malicious
 760 spikes and dips in first and higher-order topographic derivatives used by different models.
 761 A generally practiced method to avoid this issue is a smoothing approach [*Saco et al.,*
 762 *2006; Pelletier and Rasmussen, 2009*]. We here smooth the DEM prior to application of
 763 the DTB model using

$$764 \quad Z_{i,j}^k = [Z_{i,j}^{k-1} + w (Z_{i,j-1}^{k-1} + Z_{i,j+1}^{k-1} + Z_{i-1,j}^{k-1} + Z_{i+1,j}^{k-1})] / (1 + 4w), \quad (19)$$

765 where $Z_{i,j}$ = elevation of a spatial location given by coordinates i and j [L]; k = iteration;
766 and w = empirical weight [-]. The degree of smoothing can be controlled by the iteration
767 number k and by $w \in (0, 1]$. The exact value of the weight is not particularly important as
768 the degree of smoothing can be controlled by iteration number. The smaller the value of
769 the weight the more iterations are required to reach a certain smoothed topography. The
770 number of iterations required to remove small-scale topographic imperfections depends
771 on the accuracy of the LiDAR observations, and is thus data set dependent.

772 To better understand how the number of iterations affects the smoothed topographic,
773 please consider Figure 8 which plots the outcome of Equation (19) for different values of
774 k and $w = 0.2$ using a cross section of the DEM of the PRB. The top panel plots the
775 topographic surface for values of $k = 5$ (blue), $k = 10$ (green), $k = 30$ (red) and $k = 50$
776 (cyan). The original LiDAR measured (non-smoothed) surface is separately indicated
777 with the dashed black line. The large black rectangles are zoomed insets of the smaller
778 rectangles of the footslope (depositional area) and sideslope (steepest gradient) and much
779 better demonstrate the effect of the different iterations on the topographic surface. A few
780 iterations (5 to 10) with the smoothing kernel of Equation (19) is sufficient to remove
781 the small-scale defects (roughness) so clearly visible in the insets but does not affect the
782 main properties of the DEM. The use of a larger number of iterations ($k > 10$) compro-
783 mises unnecessarily the DEM and introduces topographic discrepancies in the drainage
784 and hilltop regions of the hillslope. In summary, a value of $k \in [5, 10]$ is sufficient to
785 correct for small-scale topographic imperfections and maintains the overall integrity and
786 characteristics of the measured DEM. For other values of $w \in (0, 1]$ the same analysis can
787 be repeated to determine a suitable value for k .

788 Different approaches have been used in the literature to remove the pit-and-mound
789 topography captured by LiDAR DEM but also retain the hillslope scale pattern [*Saco*
790 *et al.*, 2006; *Pelletier and Rasmussen*, 2009]. Recent studies have attempted to extract
791 relevant scales for smoothing high-resolution surfaces [*Roering et al.*, 2010; *Hurst et al.*,
792 2012]. However, a discussion about different smoothing methods is outside the scope of
793 the present paper and we refer to these publications for further information. We now use
794 the smoothed DEM as input to DTB model and fit the model against observed bedrock
795 depth data using a lumped and distributed parameterization with the DREAM algorithm.

6.3. DTB Model with Lumped Parameter Values

796 The method proposed in section 5.1 is now applied to the borehole observations at the
797 experimental site. The bedrock data set is split randomly into two parts, designated for
798 DTB-model calibration (75%) and evaluation (25%). The observations that were affected
799 by tree roots and boulders were removed from the data set. A pixel size of the DEM
800 of 4 m was deemed an acceptable trade-off between model accuracy and computational
801 efficiency. We now estimate the posterior distribution of the DTB model parameters,
802 $\theta = \{\Phi, \lambda_1, \lambda_2, S_c\}$ using Bayesian inference with DREAM. The prior ranges for the
803 parameters are listed in Table 4. We now discuss the results.

804 Figure 9 presents a scatter plot matrix of the posterior samples derived from DREAM.
805 The graphs on the main diagonal present marginal distributions of each of the parameters,
806 whereas the off-diagonal elements display bivariate scatter plots of the posterior samples.
807 The posterior distribution of the parameter Φ follows closely a normal distribution with
808 median posterior solution that is in excellent agreement with the MAP value, separately
809 indicated in the histogram with the blue cross symbol (A). The posterior histogram of

810 Φ has many elements in common with its counterpart derived in the synthetic study
811 case (Figure 9(A)). Indeed, the marginal distribution extends only a small portion of the
812 uniform prior distribution, which demonstrates that this parameter is well defined by
813 calibration against the real-world bedrock depth data. The marginal distributions of the
814 other three parameters occupy almost their entire prior distribution, which suggest that
815 these parameters are poorly defined by calibration against our bedrock depth observations.
816 The relatively low values of the MAP value of parameter λ_1 suggests that the bedrock
817 is close to the surface in the channel zone with a thin soil mantle overlying a weathered
818 bedrock zone (Figure 9(F)). The high MAP value for λ_2 (Figure 9(K)) signifies that the
819 bedrock valley topography approximates a smooth concave shape (see Figure 1). The
820 marginal distribution of parameter S_c is quite different from its synthetic case (Figure
821 9(P)). Indeed, S_c now attains much higher values, demonstrating the presence of a much
822 thicker regolith zone underneath steep slopes. The bivariate scatter plots (off-diagonal)
823 highlight the presence of some negligible correlation between the DTB parameters, Φ and
824 λ_2 and Φ and S_c as in section 5.1.

825 The posterior mean parameter values derived from the calibration are now used to de-
826 termine the performance of the DTB model on the independent evaluation data set. The
827 performance of the DTB model is summarized in Table 5. The listed value of the RMSE
828 of 1.80 m and the ρ -statistic of 0.83 can be considered acceptable for the PRB experi-
829 mental watershed. These performance metrics might be improved upon if a distributed
830 parameterization of the DTB model is used. We therefore turn our attention again to the
831 assumption that the parameter Φ might contain information about rock heterogeneity not

832 explicitly accounted for in the DTB model formulation. We discuss the results of such
833 distributed parameterization in the next section.

6.4. DTB Model with Spatially Distributed Parameter Values

834 In a previous section of this paper we have shown (see Fig. 1) that the DTB model
835 simulates a smooth bedrock surface from the hilltop to the drainage channel in the val-
836 ley. Such regular surface does not do justice to the rather dynamic variations of the
837 regolith thickness at different experimental sites in Rio de Janeiro. This DTB variability
838 is partly explained by measurement errors of the dynamic cone penetrometer but cannot
839 be described and mimicked accurately with an analytic solution. The assumptions of the
840 DTB model are convenient in deriving analytic solutions of the bedrock surface but might
841 not characterize adequately three-dimensional topographic effects arising from ridge and
842 valley topography and vertical or lateral heterogeneities, particularly the K/ϕ relation
843 [*Rempe and Dietrich, 2014*]. What is more, the channel incision rate, C_0 is unlikely to be
844 constant over large timescales, due to (among others) a variably bedrock resistance, lat-
845 eral movement of the channel, and internal dynamics of stream capture at the PRB field
846 site. Furthermore, the bedrock is assumed to be spatially homogeneous and rock mass
847 discontinuities are ignored. These processes (and properties) are very difficult to charac-
848 terize adequately with an analytic solution, and instead warrants numerical modeling of
849 the bedrock depth.

850 We now discuss the results of the DTB model for two different distributed parameter
851 cases. In the first trial, a different value of Φ is assumed for each sub watershed of the PRB,
852 and the other three parameters (λ_1 , λ_2 and S_c) assume lumped values over the domain of
853 interest (Figure 4). This involves the inference of $d = 5$ parameters. In the second trial,

854 all four DTB-model parameters are varied per sub catchment within the PRB, thereby
855 increasing further the model complexity to $d = 8$. Figure 10 presents the evolution of the
856 sampled \hat{R} -values for each DTB model parameters of the distributed parameterization
857 with $d = 8$. About 10,000 DTB model evaluations are required for DREAM to converge
858 successfully to a stationary distribution. This requires a few minutes of calculation on a
859 standard laptop computer. Parallel computing can be used to reduce further the CPU-
860 budget.

861 Table 5 summarizes the performance statistics of the two distributed parameterizations
862 for the evaluation data set. The listed RMSE and ρ -statistics appear very similar with
863 RMSE that has decreased from 1.80 m for the lumped case to 1.76 m for both distributed
864 parameterizations. The ρ -statistic appears rather unaffected and actually has deteriorated
865 somewhat from 0.83 to 0.82 when the number of parameters is increased beyond four
866 (lumped case) or five (first distributed case). The distributed parameterization of the
867 DTB model with $d = 5$ receives the lowest value of the AIC metric, and is thus most
868 supported by the available soil depth data. This value of 191.10 is somewhat lower than
869 its counterpart of 194.00 and 193.90 for the lumped and most distributed parameter case,
870 respectively. Altogether, we conclude that the distributed parameterization with $d = 5$ is
871 statistically preferred.

872 We now plot in Figure 11 the DTB simulated regolith thicknesses at the PRB ex-
873 perimental watershed using the mean posterior solution of the lumped (A: $d = 4$) and
874 distributed parameterizations (C: $d = 5$; E: $d = 8$). To simplify graphical interpretation,
875 a common color bar is used for all three calibration cases. The scatter plots at the right
876 hand side compare the observed and simulated regolith depth values at the different mea-

877 surement locations. The solid black line is used to denote the identity or 1:1 line. The
878 color coding in these regression plots matches the color bar used in the figures at the left
879 hand side. The simulated bedrock depth maps of the different calibration cases appear
880 very similar and exhibit only small differences if a distributed parameterization is used.
881 The DTB model predicts a smooth topography from the hilltop (thick regolith) to the
882 drainage channel (thin or even exposed rock), a pattern that agrees well with field obser-
883 vations. These results are in agreement with theory [*Rempe and Dietrich, 2014; Clair et*
884 *al., 2015*] and field expertise [*Liang and Uchida, 2014; Kim et al., 2015*] for a geologically
885 similar environment with steep slopes on a granitic rock mass, and provides support for
886 the claim that the DTB model gives an adequate description of the bedrock surface at
887 the PRB field site.

888 We conclude this section with Figure 12, which plots the DTB simulated bedrock pro-
889 file of the mean posterior solution for the **BB'** transect (Figure 7) using the distributed
890 ($d = 5$) parameterization. The topographic surface is indicated with the black line and
891 the observed bedrock depth data are indicated separately with a blue dot. The dark gray
892 region represents the 95% confidence intervals of the output prediction due to parameter
893 uncertainty, whereas the light gray region denotes the corresponding total prediction un-
894 certainty. The simulated posterior mean bedrock surface (solid red line) appears rather
895 smooth and fits nicely the observed bedrock depth observations. The 95% parameter
896 uncertainty bounds appear relatively small and track closely the observed regolith depth
897 data. The total (model + parameter) 95% prediction uncertainty intervals are rather
898 large and encompass the observations. The different DTB model parameterizations pre-

dict a very similar posterior mean bedrock depth surface (not shown), but the prediction uncertainty increases (as expected) with increasing dimensionality of the parameter space.

7. DISCUSSION

The Bayesian inversion framework used herein enables synthesis of geomorphic models with spatially distributed field observations. This approach uses MCMC simulation with DREAM to search efficiently the model parameter space in pursuit of so called posterior samples that honor best the observed data. The quality of fit is quantified by a likelihood function which takes into explicit account the calibration measurement data error. A prior distribution can be used to constrain the ranges of each parameter and/or to favor values in better agreement with yet available geologic data. The posterior samples of DREAM are then visualized using marginal distributions and pairs of bivariate scatter plots. These plots can be used to assess parameter sensitivity and correlation. Predictive uncertainty can be assessed by evaluating the model with each posterior parameter solution. The posterior mean simulation can then be compared to validation data to benchmark the performance of the model and help verify the main assumptions and equations it is based on. This step is an integral part of the scientific method and key to model (hypothesis) refinement.

The DREAM algorithm is designed specifically to solve for the target distribution in high-dimensional parameter spaces. Parameters whose marginal distribution is relatively tight appear well-resolved by the available data. If, on the contrary, the marginal distribution occupies a large portion of the prior distribution, then the parameter cannot be constrained by the calibration data and can be classified as insensitive. The use of spatially distributed parameter values provides a means to account implicitly, and in a

921 relatively simple way, for system heterogeneities that are difficult, or sometimes impossi-
922 ble, to characterize adequately in the field. For example, the DTB model can simulate
923 spatially varying $\phi C_o/K$ if the value of Φ is varied over the watershed of interest. One
924 should be particularly careful however not to use too many distributed parameters to
925 characterize spatially the geomorphic processes and bedrock properties of the watershed of
926 interest as this increases significantly the chances of overfitting. An example of this was
927 given in the first case study involving synthetically generated bedrock depth observations.
928 The closest match with the bedrock data is achieved with a distributed implementation
929 of the DTB-model involving inference of $d = 28$ parameters. The RMSE of this param-
930 eterization (1.40 m) is considerably lower than its counterpart of 1.52 m derived from a
931 lumped calibration, nonetheless a comparison of their AIC values (221.43 versus 192.30)
932 suggests that the lumped parameterization is preferred statistically. Thus among com-
933 peting hypothesis the one with the lowest value of the AIC should be selected. This
934 principle of parsimony is also known as Occam's razor. Indeed, in both our case studies
935 the simplest distributed DTB-model parameterization ($d = 5$ for the real-world case) is
936 most supported by the available soil depth data.

937 Bayesian analysis coupled with MCMC simulation has several key advantages over stan-
938 dard optimization approaches, one of which is the explicitly characterization of model sim-
939 ulation (prediction) uncertainty. The depth to bedrock, for instance, is a key input vari-
940 able in hydromechanical and geotechnical studies, but without underlying estimates of
941 uncertainty, this boundary is treated instead as a fixed entity in slope stability analysis
942 and debris-flow studies [*Guimarães et al.*, 2003; *Fernandes et al.*, 2004; *Gomes et al.*,
943 2008, 2013]. As the posterior mean simulation of the bedrock depth underneath the hill-

944 slope or watershed was shown to be in excellent agreement with the observed data, the
945 DTB model output should improve considerably simulation of large-scale shallow land-
946 slides and debris-flow events [*Gomes et al.*, 2013]. What is more, we can also propagate
947 forward the bedrock depth uncertainty through hydromechanical models to quantify pre-
948 diction intervals of key output variables such as landslide potential and factor of safety.
949 The availability of an accurate bedrock depth map also makes it easier to characterize
950 adequately the impact of soil hydraulic and soil strength properties on slope stability. Pre-
951 vious work at the PRB published in *Guimarães et al.* [2003] treated bedrock topography
952 and soil cohesion as a single variable controlling shallow landslides.

953 A lumped parameterization of the DTB model is warranted for a sparse data set of
954 regolith depth observations. The number of degrees of freedom, $df = n - d$ then remains
955 sufficiently large to minimize the chances of overfitting. If a sufficiently large number of
956 bedrock depth measurements is available, then a distributed DTB model parameterization
957 can be used. The most promising results for the PRB were derived if the parameter Φ
958 is varied spatially per sub catchment. The parameter S_c enables simulation of varying
959 bedrock depths along the hillslope and allows the DTB model as proposed herein to
960 reproduce accurately the presence of thin soils and/or exposed rock at the steep slopes
961 in the upland portion of the PRB. The bedrock-valley morphology in the DTB model is
962 controlled by the variable Λ and inference of its parameters λ_1 and λ_2 allows simulation of
963 many different shapes and depths of the bedrock surface underneath the drainage channel.

964 In this paper we have used spatially distributed observations of the bedrock depth as
965 a calibration target. This integrated variable summarizes the cumulative history of a
966 myriad of different geologic processes such as climate cycles, internal dynamic, episodic

967 instabilities (mass movements), variable resistant rock mass and nonuniform channel in-
968 cision [Rempe and Dietrich, 2014]. These processes act together in the watershed, and
969 their complex (nonlinear) relationships with surface topography, soil and/or rock mass
970 properties give rise to a spatially variable bedrock depth. By using observations of the
971 bedrock depth at different locations in the watershed we can constrain sufficiently the
972 parameters (and output) of the DTB model, yet other data types are needed to verify
973 whether the processes simulated by the model are adequately described. Without such
974 data it will be very difficult to benchmark the adequacy of the different components of
975 the DTB-model in pursuit of epistemic errors. It is not particularly difficult to adapt the
976 likelihood function of Equation (14) to include other calibration data types as well.

977 If the main application of our DTB model is to produce accurate maps of the bedrock
978 depth for geotechnical analysis, then model adequacy is not as important as long as the
979 simulated bedrock depths are in reasonable agreement with their point observations. High-
980 fidelity and high-resolution bedrock depth maps can then be generated (with estimates of
981 uncertainty) using a distributed parameterization of the DTB model. This does require
982 the availability of a relatively dense network of borehole/geophysical observations and
983 careful analysis of overfitting using split sampling and/or uncertainty analysis of the pos-
984 terior maps sampled with DREAM. The simulation result of such distributed calibration
985 approach was plotted in Figure 12 using a different gray color for the DTB parameter and
986 model uncertainties. This posterior simulation of the bedrock depth can now be used for
987 probabilistic geotechnical analysis to derive 95% uncertainty intervals of common metrics
988 of slope stability and landslide potential. This framework embraces the conclusions of
989 *Catani et al.* [2010], who used an infinite slope stability model with distributed bedrock

990 depths and found that the soil thickness was probably the most significant "parameter"
991 controlling the factor of safety. Indeed, one would expect the explicit treatment of bedrock
992 depth uncertainty in geotechnical analysis to improve risk analysis and decision making.

993 In this paper we have used a classical residual based likelihood function to quantify
994 the agreement between the model and observational data. This statistical measure of
995 model/data similarity is not rooted properly in geologic/geomorphic theory and has little
996 correspondence to specific behaviors of the system. This makes it very difficult to detect
997 model structural errors, our main intended goal in application of Bayesian methods. We
998 therefore recommend the use of summary metrics of the calibration data instead. These
999 statistics can be designed to measure theoretically relevant parts of system behavior, and
1000 diagnostic evaluation then proceeds with analysis of the behavioral (signature) similarities
1001 and differences between the system data and corresponding model simulation [*Gupta et*
1002 *al.*, 2008; *Vrugt and Sadegh*, 2013]. Ideally, these differences are then related to individ-
1003 ual process descriptions, and model correction takes place by refining/improving these
1004 respective components of the model. Recent work has shown that such an approach pro-
1005 vides better guidance on model malfunctioning and related issues than the conventional
1006 residual-based paradigm [*Sadegh et al.*, 2015]. The DREAM toolbox supports the use of
1007 summary statistics and diagnostic model evaluation [*Vrugt*, 2016].

1008 The focus of our study has been only on a relatively small part of the PRB. A relatively
1009 large monetary investment would be required to obtain a high-quality bedrock depth
1010 data set for the entire watershed. This would also involve significant human commitment
1011 particularly on the steepest hillslopes of the PRB which are specifically difficult to access
1012 and dangerous to measure, even for well-trained professionals.

8. SUMMARY AND CONCLUSIONS

1013 The depth to bedrock beneath soil-mantled landscapes controls a myriad of ecologic,
1014 hydrologic, geomorphologic and atmospheric processes as it influences subsurface flow
1015 paths, erosion rates, soil moisture status, water uptake by plant roots, and latent and
1016 sensible heat fluxes. As hillslope interiors are very difficult to illuminate and access,
1017 the direct measurement of the bedrock depth is rather time consuming, and much effort
1018 and human commitment would be required to characterize adequately bedrock depth
1019 variations at spatial scales of a hillslope and watershed. Thus, a computer model that
1020 can simulate high-resolution spatial maps of the depth to bedrock is of great value and
1021 importance.

1022 In this paper, we have introduced the different building blocks of a DTB model to
1023 predict the vertical extent of the weathered rock underling soil-mantled hillslopes from a
1024 high-resolution topographic map of the soil surface. Our model builds on the bottom-up
1025 control on fresh-bedrock hypothesis of *Rempe and Dietrich* [2014] and calculates the thick-
1026 ness of the weathered zone from the difference between the measured surface topography
1027 and predicted groundwater profile derived from analytic solution of the one-dimensional
1028 steady-state Boussinesq equation. Two additional terms are used in our DTB model to
1029 characterize adequately the effect of mass movement on steep hillslopes, and the shape
1030 and depth of the bedrock surface in the drainage valley. Most of the model parameters can
1031 be measured directly in the laboratory or field using experiments on soil and rock mass
1032 samples, and simulated variables can be verified using cosmogenic nuclide measurements,
1033 geophysical imaging, topographic surveying, and drilling.

1034 Bayesian analysis was used to reconcile the DTB-model predicted bedrock depths be-
1035 neath hilltops, hillslopes and valleys with field observations. This approach uses MCMC
1036 simulation with DREAM to search efficiently the model parameter space in pursuit of so
1037 called posterior samples that best mimic the observed data. The quality of fit is mea-
1038 sured by a likelihood function which summarizes in a single value the distance between
1039 the observed and simulated bedrock depths. The prior distribution summarizes all our
1040 knowledge about the model parameters before the field data is collected. This distribu-
1041 tion should honor soft data, geologic observations, field expertise and literature findings.
1042 Marginal distributions and pairs of bivariate scatter plots of the posterior samples gen-
1043 erated with DREAM are used to assess parameter sensitivity and correlation. Predictive
1044 uncertainty can be assessed by evaluating the DTB model with each posterior parame-
1045 ter solution. The posterior mean bedrock depth map can then be compared to observed
1046 data to benchmark the performance of the DTB model and help verify structural weak-
1047 nesses. This step is an integral part of the scientific method and key to model (hypothesis)
1048 refinement.

1049 Two case studies with synthetic and real-world regolith depth data from the Papagaio
1050 river basin in Rio de Janeiro, Brazil were used to illustrate the usefulness and applicability
1051 of our DTB model and methodology. Our results demonstrate that the proposed DTB
1052 model with lumped parameters mimics reasonably well the observed regolith depth data
1053 with root mean square error (RMSE) of the posterior mean simulation of 1.52 m and 1.80
1054 m for the synthetic and PRB evaluation data set, respectively. The performance of the
1055 DTB model can be enhanced if a distributed parameterization of Φ is used with RMSE
1056 for both data sets reduced to 1.47 and 1.76 m, respectively. The use of a distributed

1057 parameterization provides a means to account implicitly, and in a relatively simple way,
1058 for geologic/geomorphic watershed heterogeneities that are difficult, or impossible, to
1059 characterize adequately in the field.

1060 The DTB simulated bedrock surface underneath the watershed can be used as input to
1061 hydromechanical models and should improve considerably the reliability of hillslope scale
1062 simulations of shallow landslides and debris-flow. The posterior bedrock depth simulations
1063 of the DTB model also allow uncertainty quantification of some key output variables of
1064 hydromechanical models such as landslide potential and factor of safety. What is more,
1065 the availability of an accurate bedrock depth map also makes it easier to characterize
1066 adequately the impact of soil hydraulic and soil strength properties on slope stability.

1067 **Acknowledgments.** We appreciate the comments of the four referees that have greatly
1068 improved this manuscript. We wish to thank João Paulo Araújo and Nelson F. Fernandes
1069 for help with field work and Mojtaba Sadegh for feedback on the revision process. The first
1070 and third author greatly acknowledge research and financial support from the Brazilian
1071 National Council for Scientific and Technological Development, CNPq. The first author
1072 is also grateful to the Highway Department of Espírito Santo State in Brazil (DER-ES)
1073 for their help during this research. The MATLAB toolbox of DREAM is available upon
1074 request from the second author. This includes the setup and modeling scripts used in this
1075 paper (jasper@uci.edu).

References

1076 Akaike, H. (1974), A new look at the statistical model identification, *IEEE Transactions*
1077 *on Automatic Control*, 19(6), 716–723, doi: 10.1109/TAC.1974.1100705.

- 1078 Anderson, R. S., S. P. Anderson and G. E. Tucker (2013), Rock damage and regolith trans-
1079 port by frost: an example of climate modulation of the geomorphology of the critical
1080 zone, *Earth Surface Processes and Landforms*, *38*, 299–316, doi: 10.1002/esp.3330.
- 1081 Askarinejad, A., F. Casini, P. Bischof, A. Beck, and S. Springman (2012), Rainfall induced
1082 instabilities: a field experiment on a silty sand slope in northern Switzerland, *Rivista*
1083 *Italiana di Geotecnica*, *3*, 50–71.
- 1084 Athapaththu, A. M. R. G., T. Tsuchida, and S. Kano (2014), A new geotechnical method
1085 for natural slope exploration and analysis, *Natural Hazards*, *75*(2), 1327–1348, doi:
1086 10.1007/s11069-014-1384-0.
- 1087 Bear, J. (2013), *Dynamics of Fluids in Porous Media*, 784 pp., Dover publications, New
1088 York.
- 1089 Bellugi, D., D. G. Milledge, W. E. Dietrich, J. A. McKean, J. T. Perron, E. B. Sudderth,
1090 and B. Kazian (2015), A spectral clustering search algorithm for predicting shallow
1091 landslide size and location, *Journal of Geophysical Research: Earth Surface* , *120*(2),
1092 300–324, doi:10.1002/2014JF003137.
- 1093 Bertoldi, G., R. Rigon, and T. M. Over (2006), Impact of watershed geomorphic char-
1094 acteristics on the energy and water budgets, *Journal of Hydrometeorology*, *7*, 389–403,
1095 doi: 10.1175/JHM500.1.
- 1096 Boer, M., G. D. Barrio, and J. Puigdefábres (1996), Mapping soil depth classes in dry
1097 mediterranean areas using terrain attributes derived from a digital elevation model,
1098 *Geoderma*, *72*(1-2), 99–118, doi: 10.1016/0016-7061(96)00024-9.
- 1099 Bohidar, R. N., J. P. Sullivan, and J. F. Hermance (2001), Delineating depth to bedrock
1100 beneath shallow unconfined aquifers: A gravity transect across the Palmer river basin,

- 1101 *Groundwater*, 39, 729–736, doi: 10.1111/j.1745-6584.2001.tb02363.x.
- 1102 Borja, R. I. and J. A. White (2010), Continuum deformation and stability analyses of
1103 a steep hillside slope under rainfall infiltration, *Acta Geotechnica*, 5(1), 1–14, doi:
1104 10.1007/s11440-009-0108-1.
- 1105 Catani, F., S. Segoni, and G. Falorni (2010), An empirical geomorphology-based approach
1106 to the spatial prediction of soil thickness at catchment scale, *Water Resources Research*,
1107 46(5), doi:10.1029/2008WR007450.
- 1108 Christensen, C. W., A. A. Pfaffhuber, H. Anschütz, and T. F. Smaavik (2015), Combining
1109 airborne electromagnetic and geotechnical data for automated depth to bedrock track-
1110 ing, *Journal of Applied Geophysics*, 119, 178–191, doi: 10.1016/j.jappgeo.2015.05.008.
- 1111 Chung, J., and J. D. Rogers (2012), Estimating the position and variability of buried
1112 bedrock surfaces in the St. Louis metro area, *Engineering Geology*, 126, 37–45, doi:
1113 10.1016/j.enggeo.2011.12.007.
- 1114 Clair J. St., S. Moon, W. S. Holbrook, J. T. Perron, C. S. Riebe, S. J. Martel, B.
1115 Carr, C. Harman, K. Singha, and D. deB. Richter (2015), Geophysical imaging re-
1116 veals topographic stress control of bedrock weathering, *Science*, 350(6260), 534–538,
1117 doi: 10.1126/science.aab2210.
- 1118 Dahlke, H. E., T. Behrens, J. Seibert, and L. Andersson (2009), Test of statistical means
1119 for the extrapolation of soil depth point information using overlays of spatial environ-
1120 mental data and bootstrapping techniques, *Hydrological Processes*, 23(21), 3017–3029,
1121 doi: 10.1002/hyp.7413.
- 1122 Davis, K., and Y. Li (2011), Fast solution of geophysical inversion using adaptive mesh,
1123 space-filling curves and wavelet compression, *Geophysical Journal International*, 185(1),

- 1124 157–166, doi:10.1111/j.1365-246X.2011.04929.x.
- 1125 DeRose, R. C., N. A. Trustrum, and P. M. Blaschke (1991), Geomorphic change implied
1126 by regolith - slope relationships on steepland hillslopes, Taranaki, New Zealand, *Catena*,
1127 *18*(5), 489–514, doi: 10.1016/0341-8162(91)90051-X.
- 1128 Dietrich, W. E., R. Reiss, M. -L. Hsu, and D. R. Montgomery (1995), A process-based
1129 model for colluvial soil depth and shallow landsliding using digital elevation data, *Hy-*
1130 *drological Processes*, *9*(3-4), 383–400, doi: 10.1002/hyp.3360090311.
- 1131 Ebel, B. A., K. Loague, W. E. Dietrich, D. R. Montgomery, R. Torres, S. P. Anderson, and
1132 T. W. Giambelluca (2007), Near-surface hydrologic response for a steep, unchanneled
1133 catchment near Coos Bay, Oregon: 1. sprinkling experiments, *American Journal of*
1134 *Science*, *307*(4), 678–708, doi: 10.2475/04.2007.02.
- 1135 Eguchi, S. , M. Sawamoto, M. Masahiko (2009), Field scale determination of the
1136 aquifer–aquitard boundary in Joso Clay by cone penetrometry, *Soil Science & Plant*
1137 *Nutrition*, *55*(3), 337–348, doi: 10.1111/j.1747-0765.2009.00377.x.
- 1138 Feininger, T. (1971), Chemical weathering and glacial erosion of crystalline rocks and the
1139 origin of till, U.S. Geological Survey Professional Paper 750-C, C65–C81.
- 1140 Fernandes, N. F., A. L. Coelho Netto, and W. A. Lacerda (1994), Subsurface hydrology of
1141 layered colluvium mantles in unchannelled valleys—south-Eastern Brazil, *Earth Surface*
1142 *Processes and Landforms*, *19*, 609–626, doi: 10.1002/esp.3290190703.
- 1143 Fernandes, N. F., R. F. Guimarães, R. A. Gomes, B. C. Vieira, D. R. Montgomery, and H.
1144 Greenberg (2004), Topographic controls of landslides in Rio de Janeiro: field evidence
1145 and modeling, *Catena*, *55*(2), 163–181, doi: 10.1016/S0341-8162(03)00115-2.

- 1146 Freer, J., J. J. McDonnell, K. J., Beven, N. E., Peters, D. A. Burns, R. P. Hooper, B.
1147 Aulenbach, and C. Kendall (2002), The role of bedrock topography on subsurface storm
1148 flow, *Water Resources Research*, *38*(12), 5–1–5–16, doi:10.1029/2001WR000872.
- 1149 Fu, Z., Z. Li, C. Cai, Z. Shi, Q. Xu, and X. Wang (2011), Soil thickness effect on hydro-
1150 logical and erosion characteristics under sloping lands: A hydrogeological perspective,
1151 *Geoderma*, *167–168*, 41–53, doi: 10.1016/j.geoderma.2011.08.013.
- 1152 Fujimoto, M., N. Ohte, and M. Tani (2008), Effects of hillslope topography on hydrological
1153 responses in a weathered granite mountain, Japan: comparison of the runoff response
1154 between the valley-head and the side slope, *Hydrological Processes*, *22*(14), 2581–2594,
1155 doi: 10.1002/hyp.6857.
- 1156 Gelman, A. and D. B. Rubin (1992), Inference from iterative simulation using multiple
1157 sequences, *Statistical Science*, *7*(4), 457–472.
- 1158 Gomes, R., R. Guimarães, O. de Carvalho Jr., N. Fernandes, E. Vargas Jr., and E. Martins
1159 (2008), Identification of the affected areas by mass movement through a physically based
1160 model of landslide hazard combined with an empirical model of debris flow, *Natural*
1161 *Hazards*, *45*(2), 197–209, doi: 10.1007/s11069-007-9160-z.
- 1162 Gomes, R., R. Guimarães, O. de Carvalho Jr., N. Fernandes, and E. Vargas Jr. (2013),
1163 Combining spatial models for shallow landslides and debris-flows prediction, *Remote*
1164 *Sensing*, *5*(5), 2219–2237, doi: 10.3390/rs5052219.
- 1165 Goovaerts, P. (1997), *Geostatistics for Natural Resources Evaluation*, 1st ed., 496 pp.,
1166 Oxford Univ. Press, New York.
- 1167 Guimarães, R., D. R. Montgomery, H. M. Greenberg, N. Fernandes, R. Gomes, and O.
1168 de Carvalho Jr. (2003), Parameterization of soil properties for a model of topographic

- 1169 controls on shallow landsliding: application to Rio de Janeiro, *Engineering Geology*,
1170 *69*(1-2), 99–108, doi: 10.1016/S0013-7952(02)00263-6.
- 1171 Gupta, H. V., T. Wagener, and Y. Liu (2008), Reconciling theory with observations:
1172 elements of a diagnostic approach to model evaluation, *Hydrological Processes*, *22*(18),
1173 3802–3813, doi:10.1002/hyp.6989.
- 1174 He, M., T. S. Hogue, K. J. Franz, S. A. Margulis, and J. A. Vrugt (2011), Characterizing
1175 parameter sensitivity and uncertainty for a snow model across hydroclimatic regimes,
1176 *Advances in Water Resources*, *34*(1), 114–127, doi: 10.1016/j.advwatres.2010.10.002.
- 1177 Heimsath, A. M., W. E. Dietrich, K. Nishiizumi, and R. C. Finkel (2001), Stochastic
1178 processes of soil production and transport: erosion rates, topographic variation and
1179 cosmogenic nuclides in the Oregon Coast Range, *Earth Surface Processes and Land-*
1180 *forms*, *26*(5), 531–552, doi: 10.1002/esp.209.
- 1181 Ho, J.-Y., K. T. Lee, T. -C. Chang, Z. -Y. Wang, and Y. -H. Liao (2012), Influences
1182 of spatial distribution of soil thickness on shallow landslide prediction, *Engineering*
1183 *Geology*, *124*, 38–46, doi: 10.1016/j.enggeo.2011.09.013.
- 1184 Hopp, L. and J. McDonnell (2009), Connectivity at the hillslope scale: Identifying inter-
1185 actions between storm size, bedrock permeability, slope angle and soil depth, *Journal*
1186 *of Hydrology*, *376*(3-4), 378–391, doi: 10.1016/j.jhydrol.2009.07.047.
- 1187 Hurst, M. D., S. M. Mudd, R. Walcott, M. Attal, and K. Yoo (2012), Using hilltop
1188 curvature to derive the spatial distribution of erosion rates, *Journal of Geophysical*
1189 *Research: Earth Surface*, *117*, doi:10.1029/2011JF002057.
- 1190 Jafarpour, B. (2011), Wavelet reconstruction of geologic facies from nonlinear dynamic
1191 flow measurements, *IEEE Transactions on Geoscience and Remote Sensing*, *49*(5),

- 1192 1520–1535, doi: 10.1109/TGRS.2010.2089464.
- 1193 Jenny, H. (1941), *Factors of soil formation: A quantitative system in pedology*, 281 pp.,
1194 McGraw-Hill, New York.
- 1195 Keating, E. H., J. Doherty, J. A. Vrugt, and Q. Kang (2010), Optimization and un-
1196 certainty assessment of strongly nonlinear groundwater models with high parameter
1197 dimensionality, *Water Resources Research*, 46(10), doi:10.1029/2009WR008584.
- 1198 Kim, M. S., Y. Onda, J. K. Kim, and S. W. Kim (2015), Effect of topography and soil pa-
1199 rameterisation representing soil thicknesses on shallow landslide modelling, *Quaternary*
1200 *International*, 384, 91–106, doi: 10.1016/j.quaint.2015.03.057.
- 1201 Kosugi, K., S. Katsura, M. Katsuyama, and T. Mizuyama (2006), Water flow processes in
1202 weathered granitic bedrock and their effects on runoff generation in a small headwater
1203 catchment, *Water Resources Research*, 42(2), doi:10.1029/2005WR004275.
- 1204 Kosugi, K., Y. Yamakawa, N. Masaoka, and T. Mizuyama (2009), A combined penetrom-
1205 eter–moisture probe for surveying soil properties of natural hillslopes, *Vadose Zone*
1206 *Journal*, 8(1), doi:10.2136/vzj2008.0033.
- 1207 Kuriakose, S. L., S. Devkota, D. Rossiter, and V. Jetten (2009), Prediction of soil depth
1208 using environmental variables in an anthropogenic landscape, a case study in the West-
1209 ern Ghats of Kerala, India, *Catena*, 79(1), 27–38, doi: 10.1016/j.catena.2009.05.005.
- 1210 Laloy, E., N. Linde, and J. A. Vrugt (2012), Mass conservative three-dimensional water
1211 tracer distribution from Markov chain Monte Carlo inversion of time-lapse ground-
1212 penetrating radar data, *Water Resources Research*, 48(7), doi:10.1029/2011WR011238.
- 1213 Laloy, E., B. Rogiers, J. A. Vrugt, D. Mallants, and D. Jacques (2013), Efficient posterior
1214 exploration of a high-dimensional groundwater model from two-stage Markov chain

- 1215 Monte Carlo simulation and polynomial chaos expansion, *Water Resources Research*,
1216 *49*(5), 2664–2682, doi:10.1002/wrcr.20226.
- 1217 Lanni, C., M. Borga, R. Rigon, and P. Tarolli (2012), Modelling shallow landslide sus-
1218 ceptibility by means of a subsurface flow path connectivity index and estimates of soil
1219 depth spatial distribution, *Hydrology and Earth System Sciences*, *16*(11), 3959–3971,
1220 doi:10.5194/hess-16-3959-2012.
- 1221 Lanni, C., J. McDonnell, L. Hopp, and R. Rigon (2013), Simulated effect of soil depth
1222 and bedrock topography on near-surface hydrologic response and slope stability, *Earth*
1223 *Surface Processes and Landforms*, *38*(2), 146–159, doi: 10.1002/esp.3267.
- 1224 Lebedeva, M. I. and S. L. Brantley (2013), Exploring geochemical controls on weathering
1225 and erosion of convex hillslopes: beyond the empirical regolith production function,
1226 *Earth Surface Processes and Landforms*, *38*, 1793–1807, doi: 10.1002/esp.3424.
- 1227 Liang, W. -L. and T. Uchida (2014), Effects of topography and soil depth on saturated-
1228 zone dynamics in steep hillslopes explored using the three-dimensional Richards’ equa-
1229 tion, *Journal of Hydrology*, *510*, 124–136, doi: 10.1016/j.jhydrol.2013.12.029.
- 1230 Linde, N. and J. A. Vrugt (2013), Distributed soil moisture from crosshole ground-
1231 penetrating radar travel times using stochastic inversion, *Vadose Zone Journal*, *12*(1),
1232 doi: 10.2136/vzj2012.0101.
- 1233 Liu, J., X. Chen, H. Lin, H. Liu, and H. Song (2013), A simple geomorphic-based
1234 analytical model for predicting the spatial distribution of soil thickness in head-
1235 water hillslopes and catchments, *Water Resources Research*, *49*(11), 7733–7746,
1236 doi:10.1002/2013WR013834.

- 1237 Lochbühler, T., S. J. Breen, R. L. Detwiler, J. A. Vrugt, and N. Linde (2014), Probabilistic
1238 electrical resistivity tomography of a CO₂ sequestration analog, *Journal of Applied*
1239 *Geophysics*, *107*, 80–92, doi:10.1016/j.jappgeo.2014.05.013.
- 1240 Lochbühler, T., J. A. Vrugt, M. Sadegh, and N. Linde (2015), Summary statistics from
1241 training images as prior information in probabilistic inversion, *Geophysical Journal In-*
1242 *ternational*, *201*(1), 157–171, doi:10.1093/gji/ggv008.
- 1243 Lucà, F., G. Buttafuoco, G. Robustelli, and A. Malafronte (2014), Spatial modelling
1244 and uncertainty assessment of pyroclastic cover thickness in the Sorrento Peninsula,
1245 *Environmental Earth Sciences*, *72*(9), 3353–3367, doi:10.1007/s12665-014-3241-6.
- 1246 Masaoka, N., K. Kosugi, Y. Yamakawa, T. Mizuyama and D. Tsutsumi (2012),
1247 Application of a combined Penetrometer-moisture probe for investigating hetero-
1248 geneous hydrological properties of a footslope area, *Vadose Zone Journal*, *11*(2),
1249 doi:10.2136/vzj2011.0064.
- 1250 Metropolis, N., A. W. Rosenbluth, M. N. Rosenbluth, A. H. Teller, and E. Teller (1953),
1251 Equation of state calculations by fast computing machines, *The Journal of Chemical*
1252 *Physics*, *21*(6), 1087–1092, doi:10.1063/1.1699114.
- 1253 Mey, J., D. Scherler, G. Zeilinger, and M. R. Strecker (2015), Estimating the fill thickness
1254 and bedrock topography in intermontane valleys using artificial neural networks, *Journal*
1255 *of Geophysical Research: Earth Surface*, *120*(7), 1301–1320, doi:10.1002/2014JF003270.
- 1256 Milledge, D. G., D. Bellugi, J. A. McKean, A. L. Densmore, and W. E. Dietrich (2014),
1257 A multidimensional stability model for predicting shallow landslide size and shape
1258 across landscapes, *Journal of Geophysical Research: Earth Surface*, *119*(11), 2481–2504,
1259 doi:10.1002/2014JF003135.

- 1260 Mukhlisin, M., M. Taha, and K. Kosugi (2008), Numerical analysis of effective soil porosity
1261 and soil thickness effects on slope stability at a hillslope of weathered granitic soil
1262 formation, *Geosciences Journal*, *12*(4), 401–410, doi:10.1007/s12303-008-0039-0.
- 1263 Odeh, I. O. A., D. J. Chittleborough, and A. B. McBratney (1991), Elucidation of soil-
1264 landform interrelationships by canonical ordination analysis, *Geoderma*, *49*(1-2), 1–32,
1265 doi:10.1016/0016-7061(91)90089-C.
- 1266 Odeh, I. O. A., A. B. McBratney, and D. J. Chittleborough (1995), Further results on pre-
1267 diction of soil properties from terrain attributes: heterotopic cokriging and regression-
1268 kriging, *Geoderma*, *67*(3-4), 215–226, doi:10.1016/0016-7061(95)00007-B.
- 1269 Ohnuki, Y., C. Kimhean, Y. Shinomiya, and J. Toriyama (2008), Distribution and charac-
1270 teristics of soil thickness and effects upon water storage in forested areas of Cambodia,
1271 *Hydrological Processes*, *22*(9), 1272–1280, doi: 10.1002/hyp.6937.
- 1272 Oware, E. K., S. M. J. Moysey, and T. Khan (2009), Physically based regularization
1273 of hydrogeophysical inverse problems for improved imaging of process-driven systems,
1274 *Water Resources Research*, *49*(10), 6238–6247, doi:10.1002/wrcr.20462.
- 1275 Pelletier, J. D. and C. Rasmussen (2009), Geomorphically based predictive map-
1276 ping of soil thickness in upland watersheds, *Water Resources Research*, *45*(9),
1277 doi:10.1029/2008WR007319.
- 1278 Pelletier, J. D., L. A. McGuire, J. L. Ash, T. M. Engelder, L. E. Hill, K. W. Leroy,
1279 C. A. Orem, W. S. Rosenthal, M. A. Trees, C. Rasmussen, and J. Chorover (2011),
1280 Calibration and testing of upland hillslope evolution models in a dated landscape:
1281 Banco Bonito, New Mexico, *Journal of Geophysical Research: Earth Surface*, *116*(F4),
1282 doi:10.1029/2011JF001976.

- 1283 Perron, J. T. (2011), Numerical methods for nonlinear hillslope transport laws, *Journal*
1284 *of Geophysical Research: Earth Surface*, 116(F2), doi:10.1029/2010JF001801.
- 1285 Pokhrel, P. and H. V. Gupta (2010), On the use of spatial regularization strategies to
1286 improve calibration of distributed watershed models, *Water Resources Research*, 46(1),
1287 doi:10.1029/2009WR008066.
- 1288 Rempe, D. M., and W. E. Dietrich (2014), A bottom-up control on fresh-bedrock to-
1289 pography under landscapes, *Proceedings of the National Academy of Sciences*, 111(18),
1290 6576–6581, doi: 10.1073/pnas.1404763111.
- 1291 Reu, J. D., J. Bourgeois, M. Bats, A. Zwertvaegher, V. Gelorini, P. D. Smedt, W. Chu, M.
1292 Antrop, P. D. Maeyer, P. Finke, M. V. Meirvenne, J. Verniers, and P. Crombé (2013),
1293 Application of the topographic position index to heterogeneous landscapes, *Geomor-*
1294 *phology*, 186, 39–49, doi: 10.1016/j.geomorph.2012.12.015.
- 1295 Roering, J. J. (2008), How well can hillslope evolution models ”explain” topography? Sim-
1296 ulating soil transport and production with high-resolution topographic data, *Geological*
1297 *Society of America Bulletin*, 120(9-10), 1248–1262, doi: 10.1130/B26283.1.
- 1298 Roering, J. J., J. W. Kirchner, and W. E. Dietrich (1999), Evidence for nonlinear, diffusive
1299 sediment transport on hillslopes and implications for landscape morphology, *Water*
1300 *Resources Research*, 35(3), 853–870, doi:10.1029/1998WR900090.
- 1301 Roering, J.J., J. A. Marshall, A. Booth, M. Mort, and Q. Jin, (2010), Evidence for biotic
1302 controls on topography and soil production, *Earth and Planetary Science Letters*, 298,
1303 183–190, doi:10.1016/j.epsl.2010.07.040.
- 1304 Ruddock, E. C. (1967) Spatial variability of rock depth in Bangalore using geostatistical,
1305 neural network and support vector machine models, *Geotechnical and Geological*

- 1306 *Engineering*, 26(5), 503–517, doi:10.1007/s10706-008-9185-4.
- 1307 Ruxton B. P. and L. Berry (1959), Residual soils of the Kumasi district in Ghana,
1308 *Géotechnique*, 17(4), 359–377, doi:10.1680/geot.1967.17.4.359.
- 1309 Saco, P. M., G. R. Willgoose, and G. R. Hancock (2006), Spatial organization of soil depths
1310 using a landform evolution model, *Journal of Geophysical Research: Earth Surface*,
1311 111(F2), doi:10.1029/2005JF000351.
- 1312 Sadegh M., J. A. Vrugt, C. Xu, and E. Volpi (2015), The stationarity paradigm revis-
1313 ited: Hypothesis testing using diagnostics, summary metrics, and DREAM_(ABC), *Water*
1314 *Resources Research*, doi: 10.1002/2014WR016805.
- 1315 Sarkar, S., A. K. Roy, and T. R. Martha (2013), Soil depth estimation
1316 through soil-landscape modelling using regression kriging in a Himalayan ter-
1317 rain, *International Journal of Geographical Information Science*, 27(12), 2436–2454,
1318 doi:10.1080/13658816.2013.814780.
- 1319 Saulnier, G.-M., K. Beven, and C. Obled (1997), Including spatially variable effective soil
1320 depths in TOPMODEL, *Journal of Hydrology*, 202(1-4), 158–172, doi:10.1016/S0022-
1321 1694(97)00059-0.
- 1322 Scharnagl, B., J. A. Vrugt, H. Vereecken, and M. Herbst (2011), Inverse modelling of in
1323 situ soil water dynamics: investigating the effect of different prior distributions of the
1324 soil hydraulic parameters, *Hydrology and Earth System Sciences*, 15(10), 3043–3059,
1325 doi:10.5194/hess-15-3043-2011.
- 1326 Shafique, M., M. van der Meijde, and S. Ullah (2011), Regolith modeling and its relation
1327 to earthquake induced building damage: A remote sensing approach, *Journal of Asian*
1328 *Earth Sciences*, 42(1-2), 65–75, doi:10.1016/j.jseaes.2011.04.004.

- 1329 Sitharam, T., P. Samui, and P. Anbazhagan (2008) Spatial variability of rock depth
1330 in Bangalore using geostatistical, neural network and support vector machine models,
1331 *Geotechnical and Geological Engineering*, 26(5), 503–517, doi:10.1007/s10706-008-9185-
1332 4.
- 1333 Stewart, M. T. (1980), Gravity survey of a deep buried valley, *Groundwater*, 18, 24–30,
1334 doi:10.1111/j.1745-6584.1980.tb03367.x.
- 1335 Tarolli, P., and G. D. Fontana (2009), Hillslope-to-valley transition morphology:
1336 New opportunities from high resolution DTMs, *Geomorphology*, 113(1-2), 47–56,
1337 doi:10.1016/j.geomorph.
- 1338 Tesfa, T. K., D. G. Tarboton, D. G. Chandler, and J. P. McNamara (2009), Modeling soil
1339 depth from topographic and land cover attributes, *Water Resources Research*, 45(10),
1340 doi:10.1029/2008WR007474.
- 1341 Thomas, M. F. (1966), Implications of Deep Weathering Patterns in Crystalline
1342 Rocks in Nigeria, *Transactions of the Institute of British Geographers*, 40, 173–193,
1343 doi:10.2307/621576.
- 1344 Troch, P.A., E. van Loon, and A. Hilberts (2002), Analytical solutions to a hillslope-
1345 storage kinematic wave equations for subsurface flow, *Advances in Water Resources*,
1346 25, pp. 637–649, doi:10.1016/S0309-1708(02)00017-9.
- 1347 Tromp-van Meerveld, H.J., and J.J. McDonnell (2006a), Threshold relations in subsurface
1348 stormflow: 1. A 147-storm analysis of the Panola hillslope, *Water Resources Research*,
1349 42, doi:10.1029/2004WR003778.
- 1350 Tromp-van Meerveld, H. J. and J. J. McDonnell (2006b), Threshold relations in sub-
1351 surface stormflow: 2. The fill and spill hypothesis, *Water Resources Research*, 42(2),

1352 doi:10.1029/2004WR003800.

1353 Tsuchida T., A. M. R. G. Athapaththu, S. Kano, and K. Suga (2011), Estimation of in
1354 situ shear strength parameters of weathered granitic (Masado) slopes using lightweight
1355 dynamic cone penetrometer, *Soils and Foundations*, 51(3), 497–512.

1356 Tye, A. M., R. L. Lawley, M. A. Ellis, and B. G. Rawlins (2011), The spatial variation of
1357 weathering and soil depth across a Triassic sandstone outcrop, *Earth Surface Processes
1358 and Landforms*, 36(5), pp. 569–581, doi:10.1002/esp.2075.

1359 Vargas Jr., E. A., R. C. Velloso, T. M. P. de Campos and L. M. Costa Filho (1990),
1360 Saturated-unsaturated analysis of water flow in slopes of Rio de Janeiro, Brazil, *Com-
1361 puters and Geotechnics*, 10(3), 247–261, doi: 10.1016/0266-352X(90)90038-W.

1362 Vieira, B. C. and N. F. Fernandes (2004), Landslides in Rio de Janeiro: The role played
1363 by variations in soil hydraulic conductivity, *Hydrological Processes*, 18(4), 791–805, doi:
1364 10.1002/hyp.1363.

1365 Vrugt, J. A. (2016), Markov chain Monte Carlo simulation using the DREAM software
1366 package: Theory, concepts, and MATLAB Implementation, *Environmental Modelling
1367 & Software*, 75, 273–316, doi:10.1016/j.envsoft.2015.08.013.

1368 Vrugt, J. A., and M. Sadegh (2013), Toward diagnostic model calibration and evalu-
1369 ation: Approximate Bayesian computation, *Water Resources Research*, 49(7), 4335–
1370 4345, doi:10.1002/wrcr.20354.

1371 Vrugt, J. A., C. J. F. ter Braak, M. P. Clark, J. M. Hyman, and B. A. Robinson
1372 (2008), Treatment of input uncertainty in hydrologic modeling: Doing hydrology back-
1373 ward with Markov chain Monte Carlo simulation, *Water Resources Research*, 44(12),
1374 doi:10.1029/2007WR006720.

- 1375 Vrugt, J., C. J. F. ter Braak, C. G. H. Diks, B. A. Robinson, J. M. Hyman, and D. Hig-
1376 don (2009) Accelerating Markov chain Monte Carlo simulation by differential evolution
1377 with self-adaptive randomized subspace sampling, *International Journal of Nonlinear*
1378 *Sciences and Numerical Simulation*, *10*(3), 273–290, doi: 10.1002/esp.3423.
- 1379 Yang, Q., and F. Zhang, Z. Jiang, W. Li, J. Zhang, F. Zeng, and H. Li (2014) Relationship
1380 between soil depth and terrain attributes in karst region in Southwest China, *Journal*
1381 *of Soils and Sediments*, *14*(9), 1568–1576, doi: 10.1007/s11368-014-0904-6.
- 1382 Wiegand, C., K. Kringer, C. Geitner, and M. Rutzinger (2013), Regolith structure analysis
1383 — A contribution to understanding the local occurrence of shallow landslides (Austrian
1384 Tyrol), *Geomorphology*, *180*(3), 5–13, doi: 10.1016/j.geomorph.2012.06.027.
- 1385 Wilford, J. and M. Thomas (2013), Predicting regolith thickness in the complex weather-
1386 ing setting of the central Mt Lofty Ranges, South Australia, *Geoderma*, *206*, 1–13, doi:
1387 10.1016/j.geoderma.2013.04.002.
- 1388 Zhou, Y. and X. Wu (1994), Use of neural networks in the analysis and interpretation of
1389 site investigation data, *Computers and Geotechnics*, *16*(2), 105–122, doi: 10.1016/0266-
1390 352X(94)90017-5.
- 1391 Zhou, W., B. F. Beck, and J. B. Stephenson (2000), Reliability of dipole-dipole elec-
1392 trical resistivity tomography for defining depth to bedrock in covered karst terranes,
1393 *Environmental Geology*, *39*(7), 760–766, doi: 10.1007/s002540050491.
- 1394 Ziadat, F. (2005), Analyzing digital terrain attributes to predict soil attributes for a
1395 relatively large area, *Soil Science Society of America Journal*, *69*(5), 1590–1599, doi:
1396 10.2136/sssaj2003.0264.

1397 Ziadat, F. (2010), Prediction of soil depth from digital terrain data by integrating
1398 statistical and visual approaches, *Pedosphere*, 20(3), 361–367, doi: 10.1016/S1002-
1399 0160(10)60025-2.

Table 1. Summary and description of the main variables of the DTB model.

Symbol	Unit	Type	Description
Z_x	[-]	Model input	Slope gradient in x direction
Z_y	[-]	Model input	Slope gradient in y direction
L_d	[L]	Model input	Drainage distance
\bar{L}_d	[-]	Model input	Normalized drainage distance
Φ	[-]	Model parameter	Equivalent to $\phi C_o/K$
λ_1	[-]	Model parameter	Bedrock-valley morphology parameter
λ_2	[-]	Model parameter	Bedrock-valley morphology parameter
S_c	[-]	Model parameter	Critical angle of slope stability

Table 2. Parameters of the synthetic topographic surface model.

Description	Symbol	Index of sine wave	
		1	2
Amplitude	ω	11,880	11,630
Frequency	β	0.012	0.012
Phase constant	χ	0.661	3.790

Table 3. Summary statistics of the bedrock depth observations of the synthetic and real-world data set used herein.

Data set	minimum [m]	maximum [m]	mean [m]	σ^\dagger [m]	n^\ddagger
Synthetic	0.13	11.60	4.36	2.97	100
Real-world	0.35	14.00	6.20	3.67	137

[†] Standard deviation.

[‡] Number of point observations.

Table 4. Prior uncertainty ranges of the DTB parameters for the artificial and observed bedrock depth data.

Range	Φ [-]	λ_1 [-]	λ_2 [-]	S_c [-]
minimum	10^{-4}	0.1	1.0	0.8
maximum	10^{-1}	3.0	20.0	1.5

Table 5. Performance statistics of the calibrated DTB model after Bayesian inversion with the DREAM algorithm. We list separately the results for the synthetic (case-study I: top) and real-world (case study II: bottom) data set of bedrock depth observations using lumped and spatially distributed parameter values. The listed values of the root mean square error (RMSE) and correlation coefficient, ρ pertain to the calibration data set for the synthetic bedrock topography and evaluation data set for the real-world regolith depth observations. The AIC values in the last column are computed with Equation (5.2) using the maximum likelihood (= MAP) values of the parameters derived from the calibration data set.

Data set	Case	Dimension (d)	RMSE [m]	ρ	AIC
Synthetic	Lumped	4	1.52	0.86	192.30
	Distributed	7	1.47	0.87	191.74
	Distributed	28	1.40	0.88	221.43
Real-world	Lumped	4	1.80	0.83	194.00
	Distributed	5	1.76	0.83	191.10
	Distributed	8	1.76	0.82	193.90

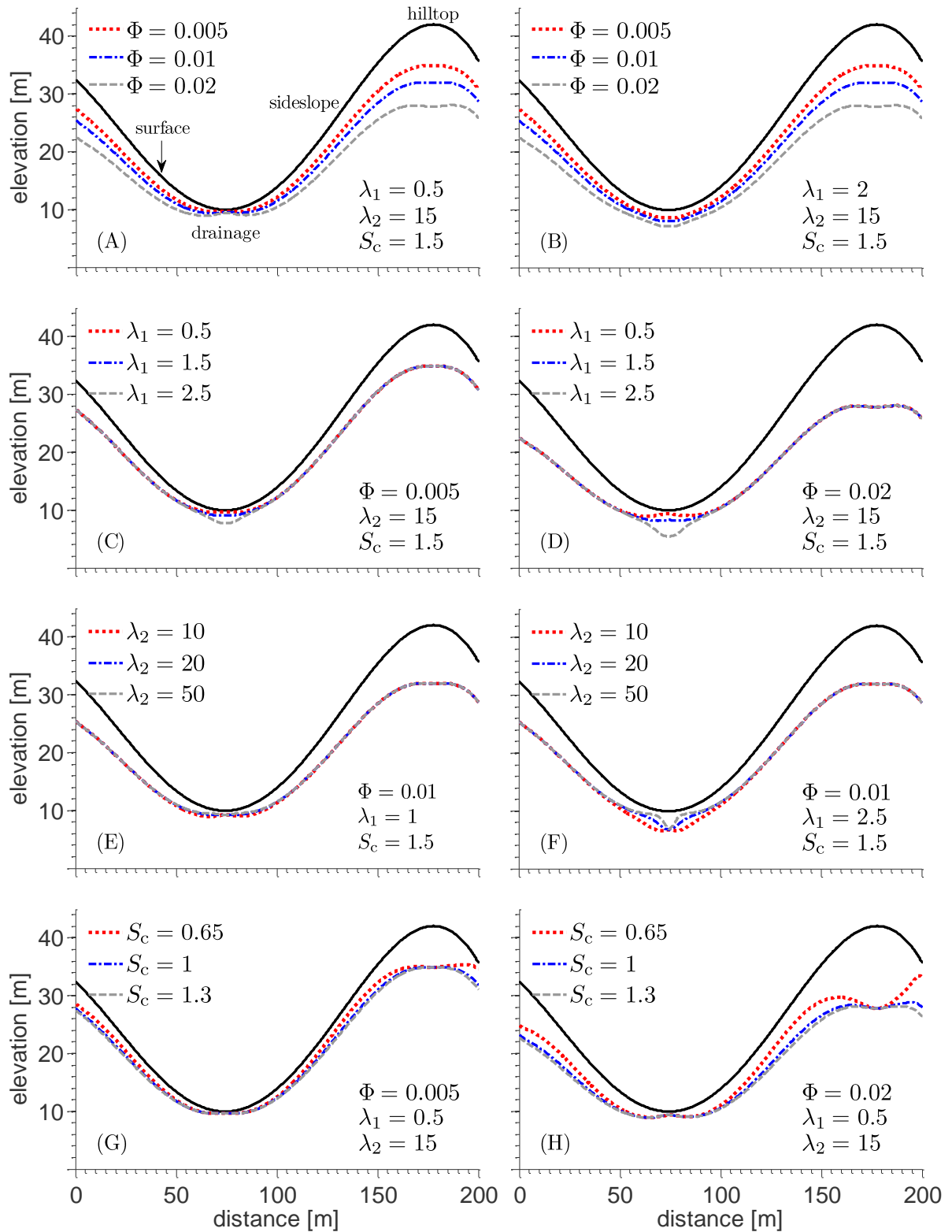


Figure 1. Sensitivity of the bedrock depth profile predicted by the DTB model to the values of the parameters Φ (A and B), λ_1 (C and D), λ_2 (E and F), and S_c (G and H). The dotted lines in red, blue, and gray display the simulated bedrock profiles for the listed values of the DTB-model parameters. The surface topography is separately indicated in each plot with the solid black line. The top-left graph (A) clarifies the position of the landscape elements "hilltop", "sideslope" and "drainage" that are used to discuss our findings.

D R A F T

January 31, 2016, 12:16am

D R A F T

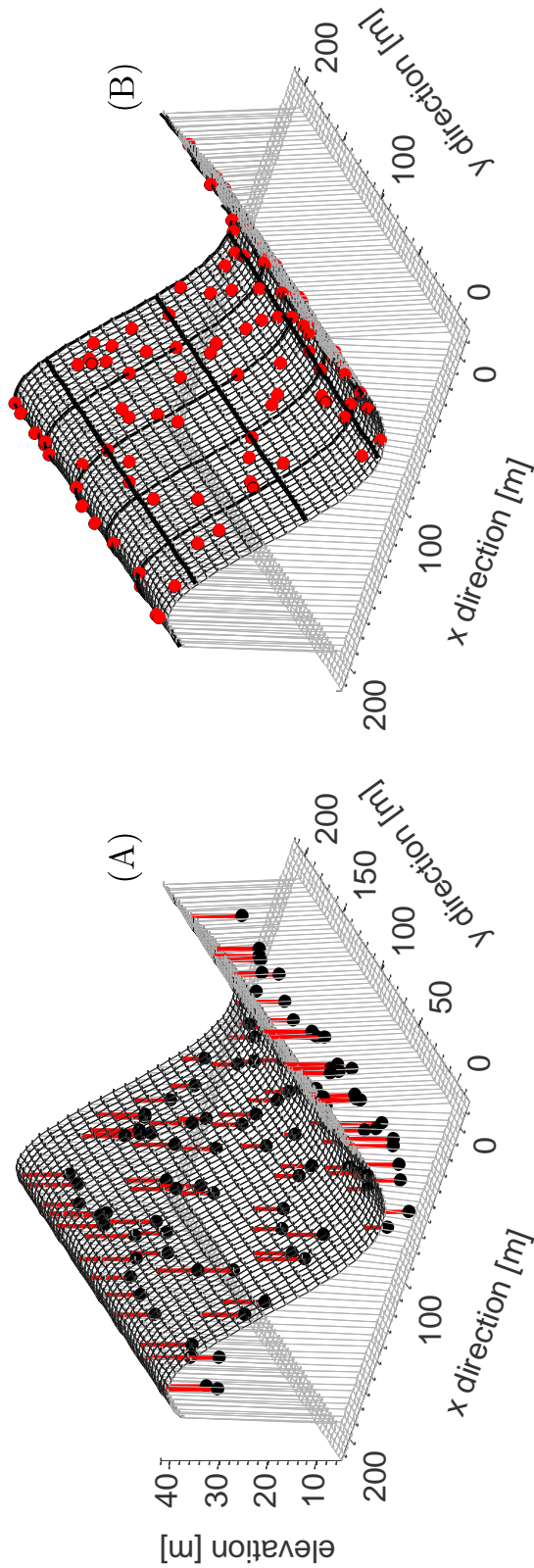


Figure 2. Plot of the synthetic topography of the spatial domain of interest, (A) boreholes (red line) that reach to the bedrock surface (black dot), and (B) measurement locations (red dots). The thin black lines represent the DEM grid with pixels (cells) of 4×4 meters, whereas the dark black lines represent the block pattern used in our distributed parameterization of the DTB model.

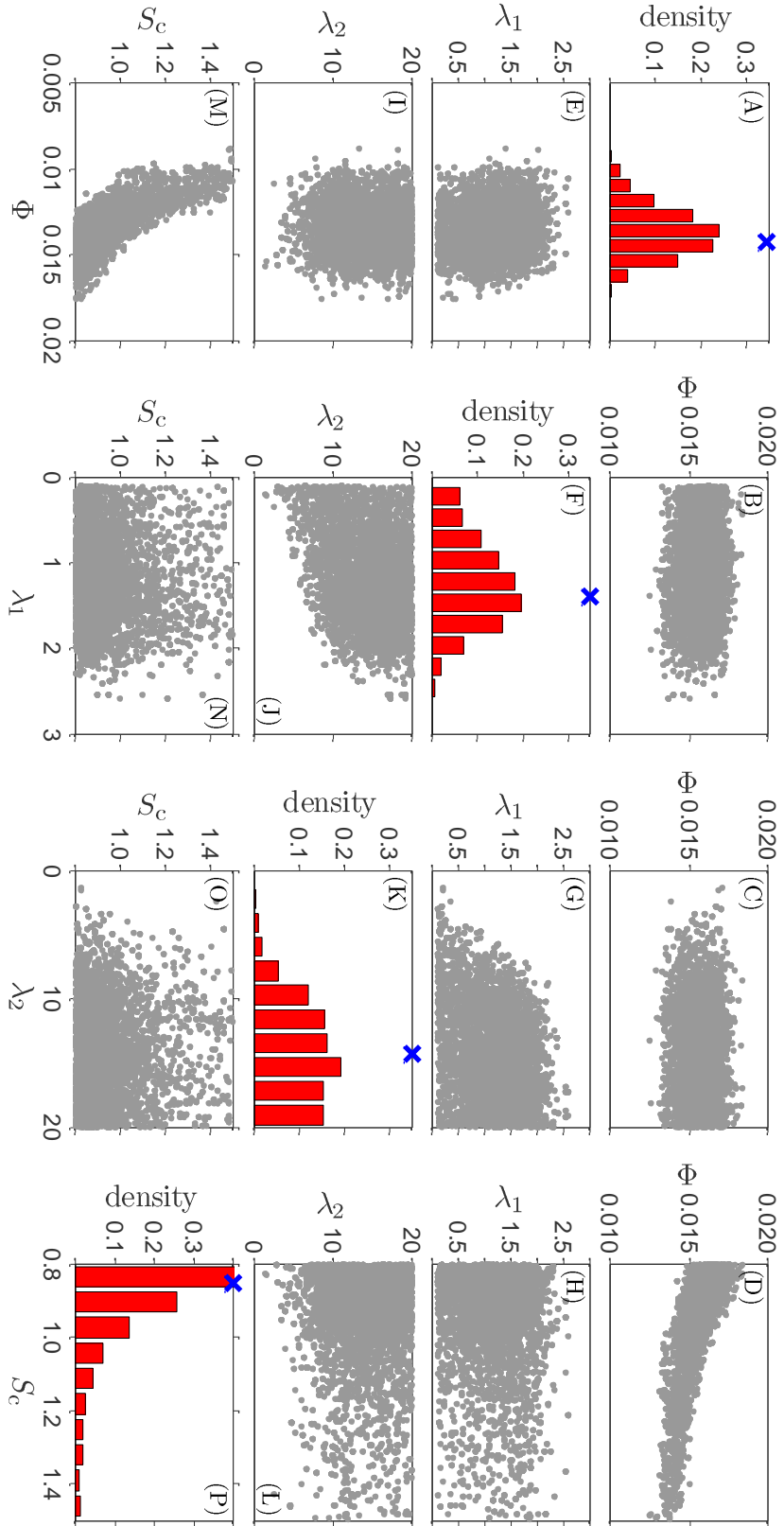


Figure 3. Lumped DTB parametrization: Scatter-plot matrix of the posterior samples generated with the DREAM algorithm. The main diagonal plots histograms of the marginal posterior distribution of the DTB model parameters, Φ , λ_1 , λ_2 and S_c , respectively, and the off-diagonal graphs present bivariate scatter plots of the posterior samples of the different parameter pairs. The MAP solution (value associated with highest likelihood) is separately indicated in each histogram with the blue cross symbol. The parameters exhibit a negligible correlation by calibration against the observed bedrock depth data.

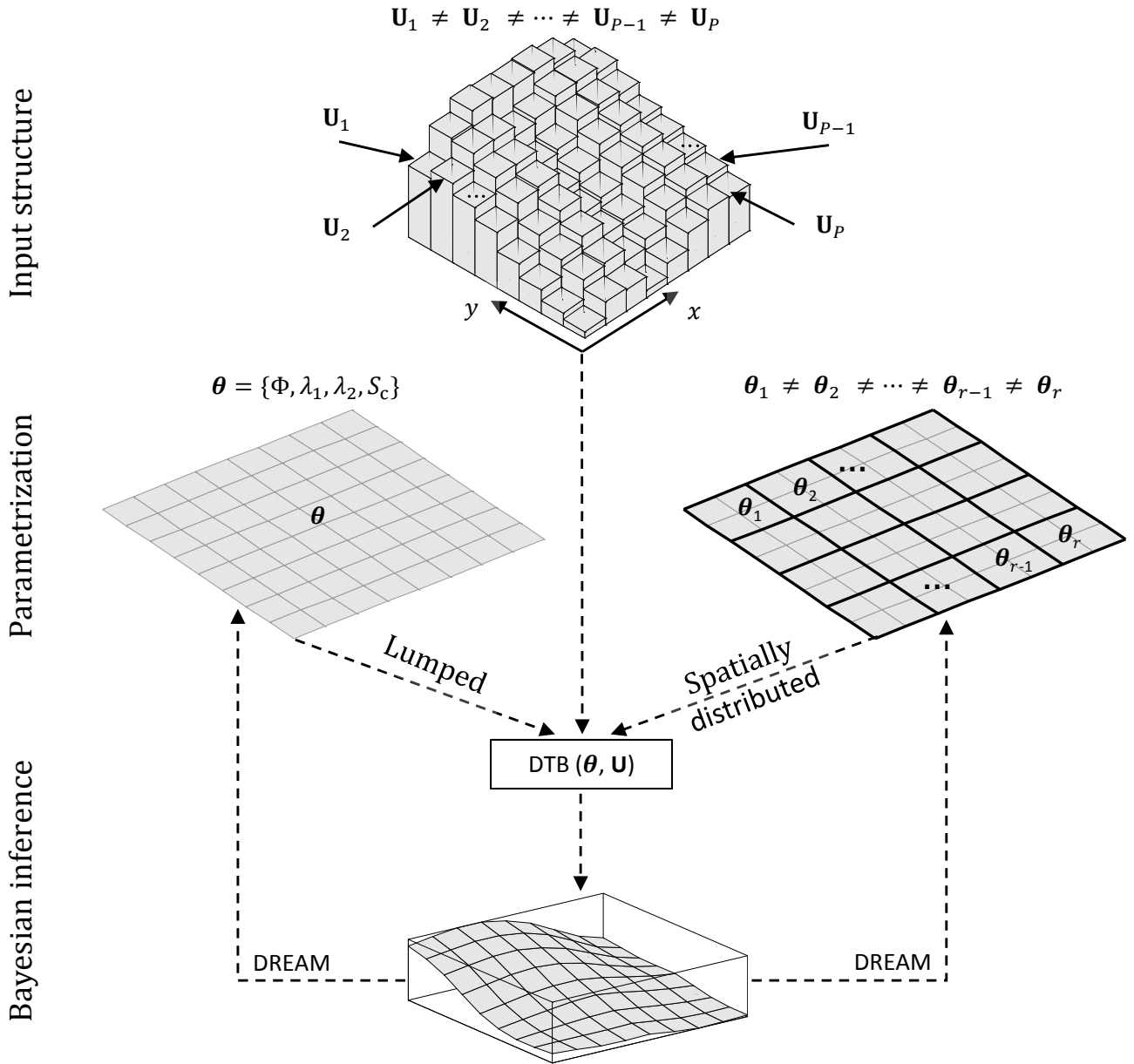


Figure 4. Schematic overview of the DTB modeling framework for a lumped (left) and distributed (right) parameterization of the watershed. The idealized DEM consists of P different grid cells and each have their own specific vector, \mathbf{U}_i , $i = \{1, \dots, P\}$, of DTB input data consisting of slope gradient and the drainage distance. The lumped (default) DTB model parameterization uses a single realization of the parameter values, $\theta = \{\Phi, \lambda_1, \lambda_2, S_c\}$ for all P grid cells of the DEM. This requires calibration of just a handful of parameters. A distributed parameterization, on the contrary, assumes different parameter values for each grid cell of the DEM. A simple block pattern is used to distribute the DTB parameters over the spatial domain of interest. The DREAM algorithm then proceeds with statistical inference of the model parameters by fitting the model to spatially distributed bedrock depth observations.

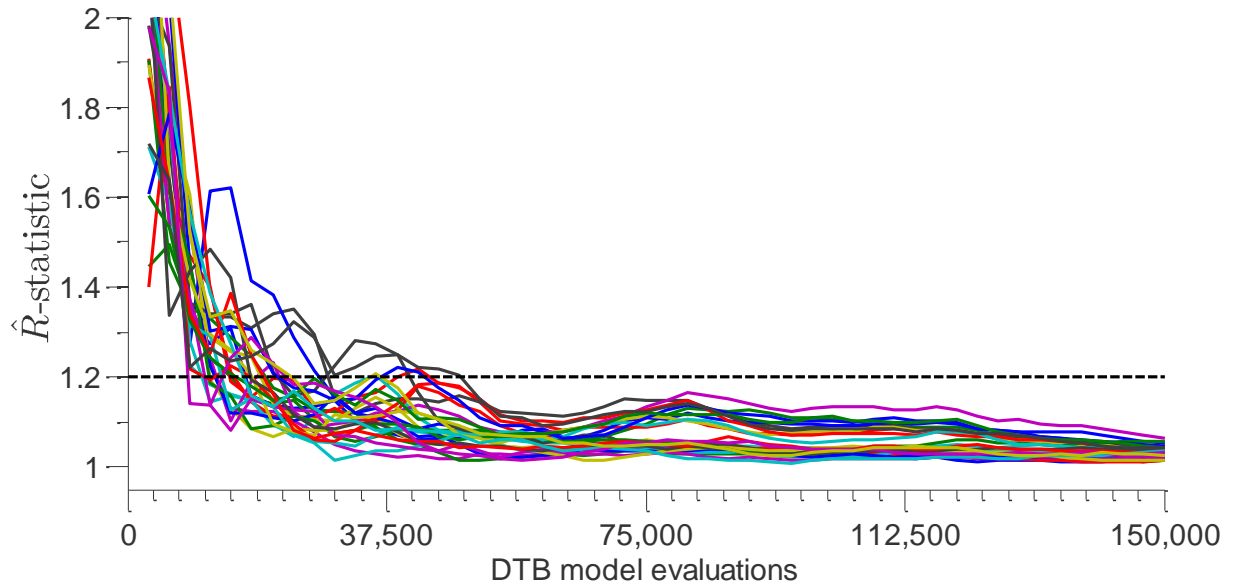


Figure 5. Distributed calibration case: Evolution of the \hat{R} -convergence diagnostic of *Gelman and Rubin* [1992] for each individual parameter of the DTB model ($d = 28$). Each parameter is coded with a different color. The dashed black line depicts the default threshold used to diagnose convergence to a limiting distribution.

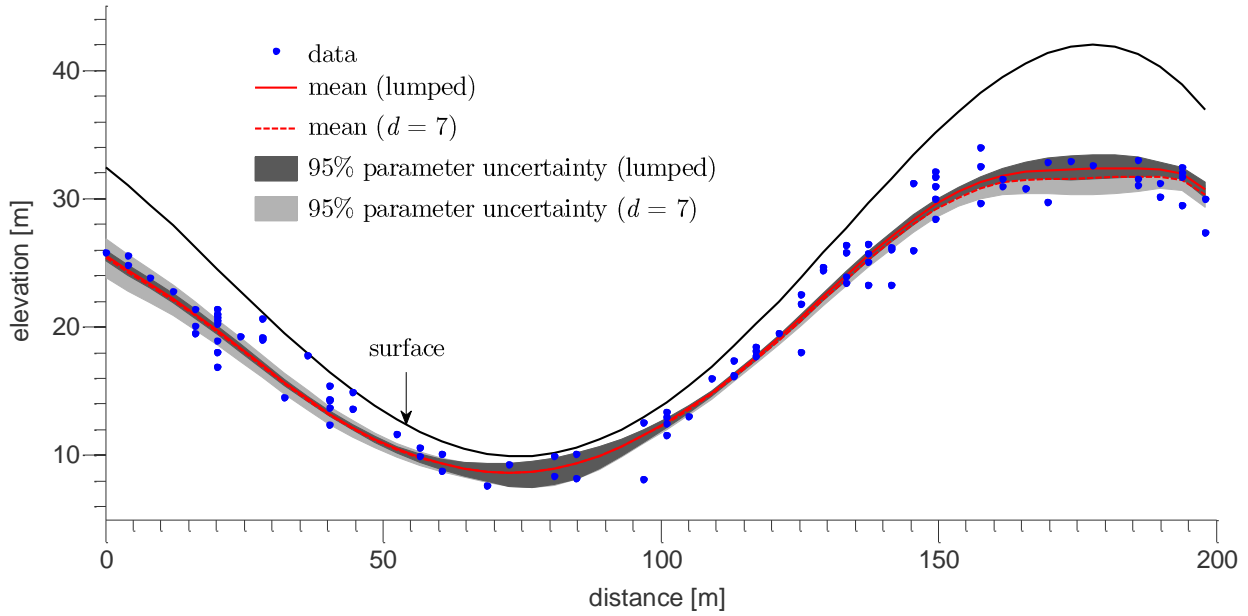


Figure 6. Lumped and distributed calibration case: Simulated bedrock surface of the DTB model for the lumped and distributed parameter case. The mean posterior solution is indicated with the solid (lumped) and dashed (distributed) red line, respectively and the light and dark gray region represent the 95% prediction intervals due to parameter uncertainty for each case. The observed bedrock depth data are separately indicated with the blue dots.

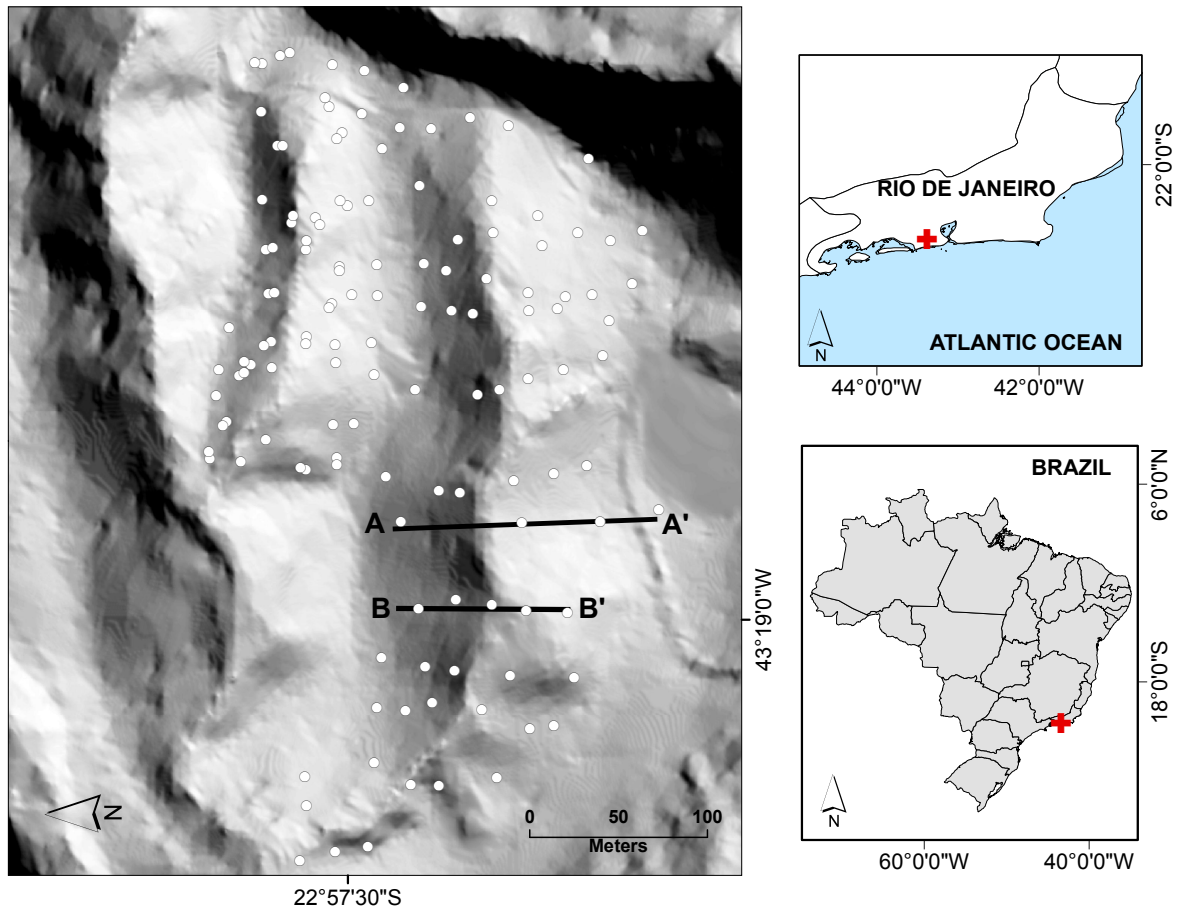


Figure 7. Geographic overview (right) and shaded relief image (left) of the PRB experimental field site in Rio de Janeiro, Brazil. The PRB field site is indicated with a red cross. The white circles (left) denote the measurement locations of the regolith depth observations using a dynamic cone penetrometer. The transect **AA'** is used to demonstrate the effects of DEM smoothing. The transect **BB'** is a cross-section in the south sub-basin and used herein to compare the simulated bedrock profile against observations of the regolith depth to unweathered bedrock.

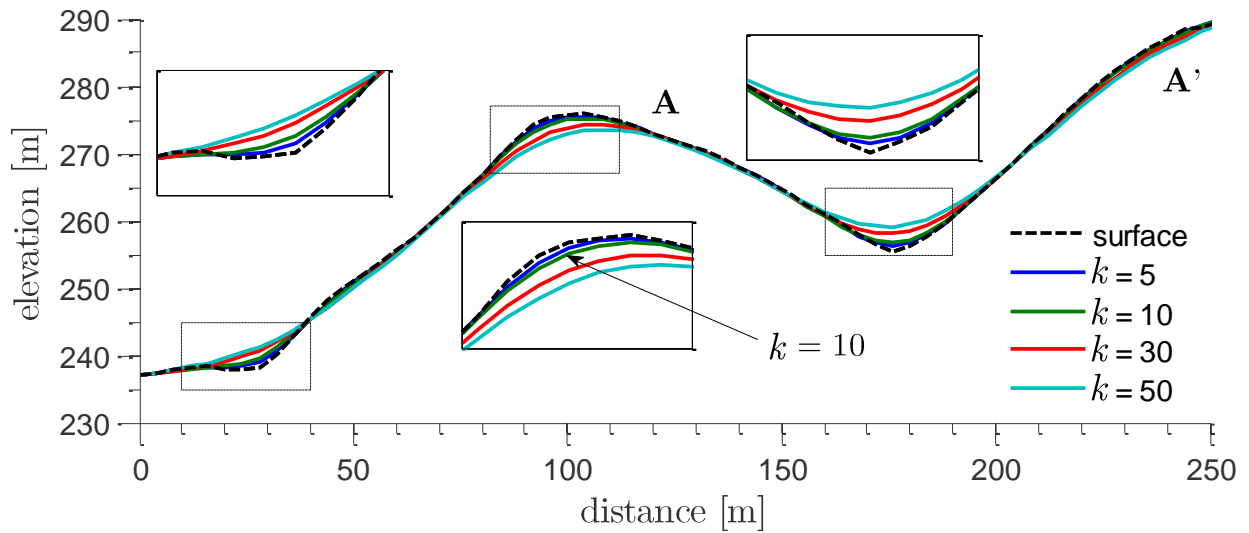


Figure 8. The effect of the number of iterations of the smoother algorithm on the topographic surface. The large black rectangles are zoomed insets of the smaller rectangles of the footslope (depositional area) and sideslope (steepest gradient). Ten iterations are deemed sufficient to remove the small topographic defects of the DEM.

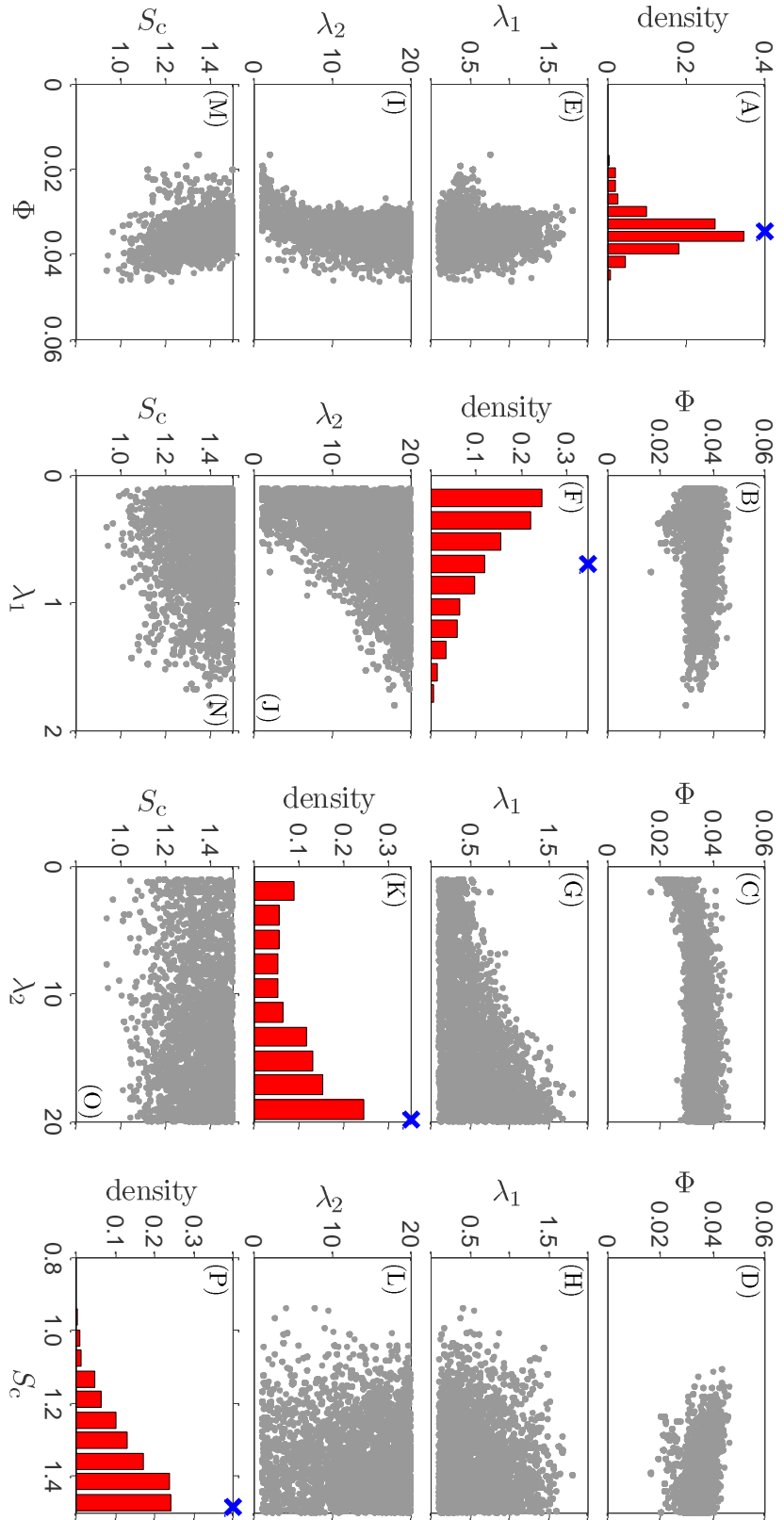


Figure 9. Lumped DTB parametrization: Scatter-plot matrix of the posterior samples generated with the DREAM algorithm. The main diagonal plots histograms of the marginal posterior distribution of the DTB model parameters, Φ , λ_1 , λ_2 and S_c respectively, and the off-diagonal graphs present scatter plots of the posterior samples of the different parameter pairs. The MAP solution (solution with highest likelihood) is separately indicated in the histograms with the blue cross symbol. The parameters pairs exhibit a negligible correlation.

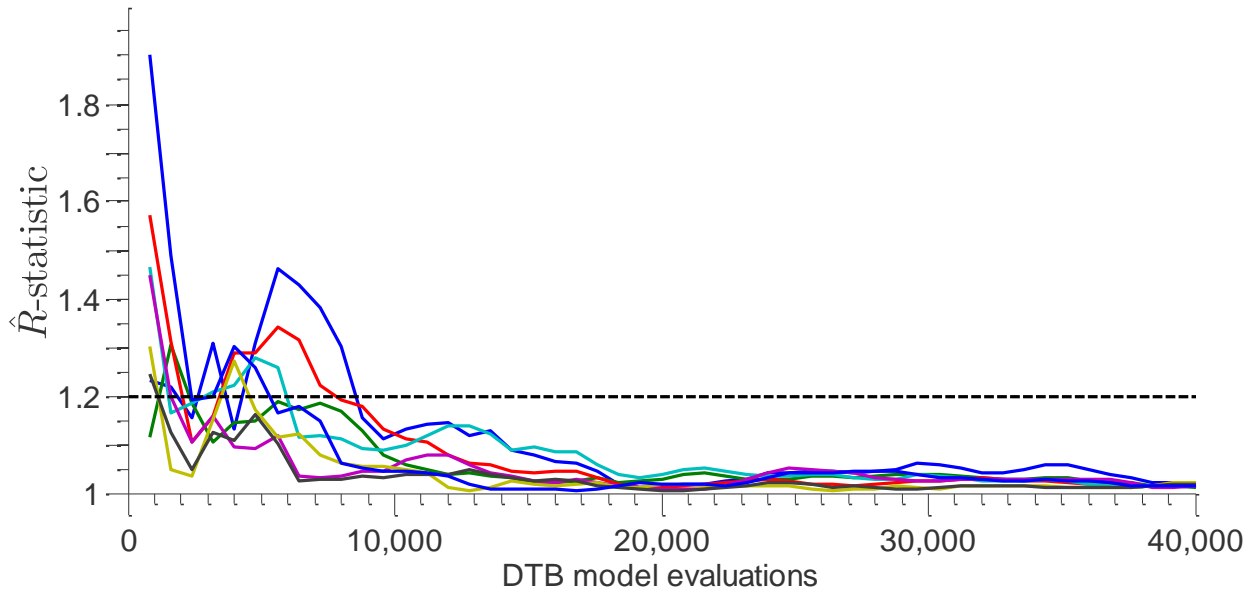


Figure 10. Distributed calibration case: Trace plot of the \hat{R} -convergence diagnostic of *Gelman and Rubin* [1992] for each individual parameter of the DTB model ($d = 8$). Each parameter is coded with a different color. The dashed black line depicts the default threshold used to diagnose convergence to a limiting distribution. About 10,000 model evaluations are needed with DREAM to converge to the posterior distribution.

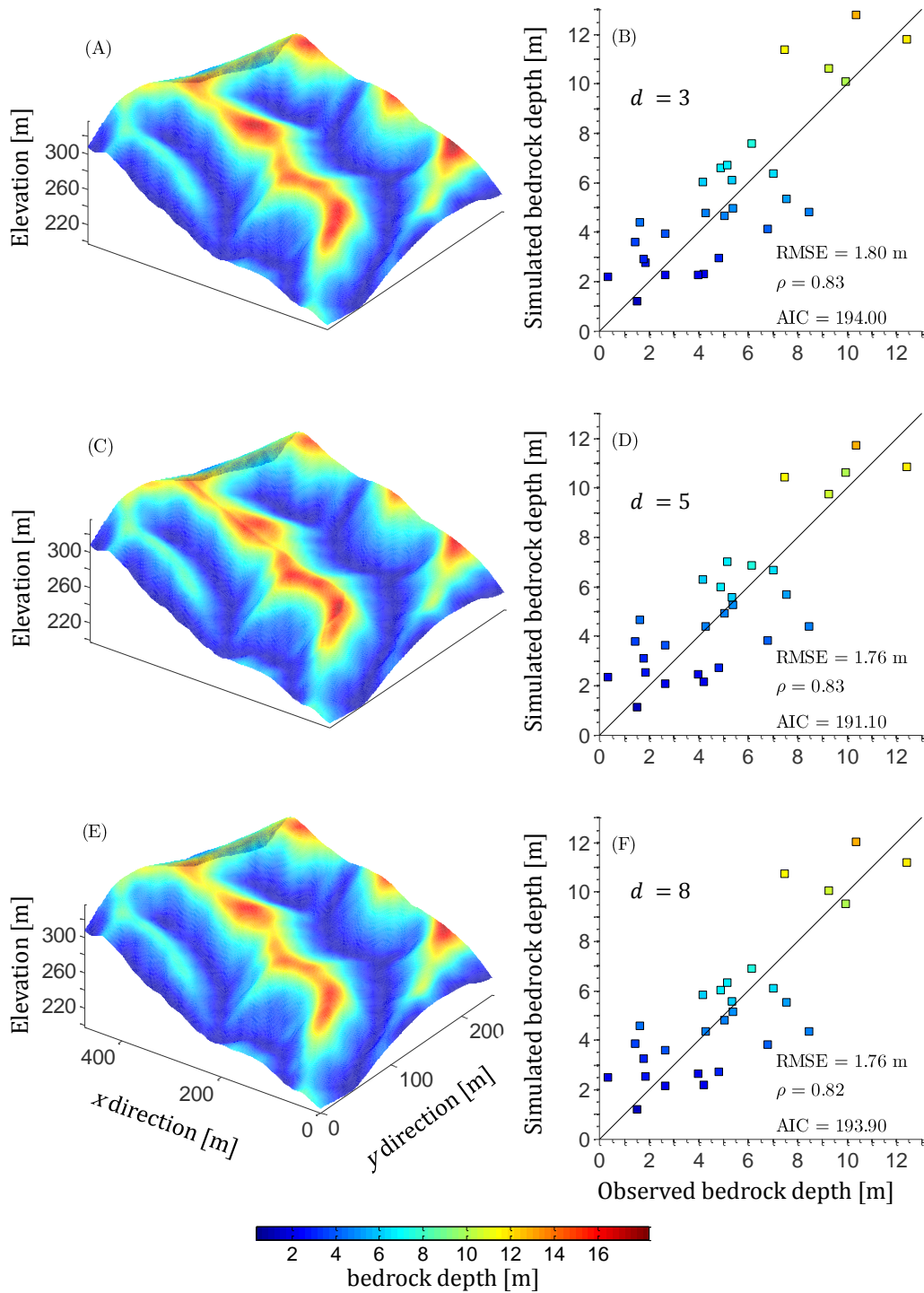


Figure 11. Lumped and distributed calibration case: Spatial distribution of the regolith thickness predicted at the PRB experimental watershed using a (A) lumped and (C,E) distributed parameterization. The DTB model predicts deep soils at the hilltop and relatively thin weathered zones in the channel, a result which is in agreement with regolith depth observations at the PRB and field expertise of hillslopes in Rio de Janeiro. The bivariate scatter plots at the right hand side compare the observed and simulated bedrock depths of the evaluation data set of the PRB. Summary statistics of the goodness-of-fit (RMSE, ρ and AIC) are listed in each plot along with the number of model parameters, d . The color coding of these regression plots matches exactly that of the bedrock depth maps.

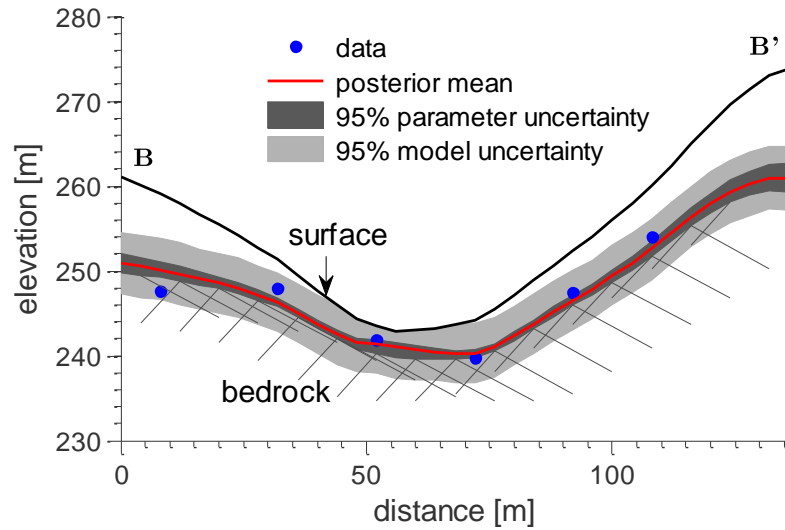


Figure 12. Distributed calibration case: Simulated DTB bedrock surface of the posterior mean solution (solid red line) derived from DREAM for the transect **BB'** at the PRB experimental watershed. The dark and light gray region plot the 95% prediction intervals due to the parameter and total simulation uncertainty. The topographic surface is indicated with the black solid line, and the observed regolith depth data are separately indicated with the blue dots.